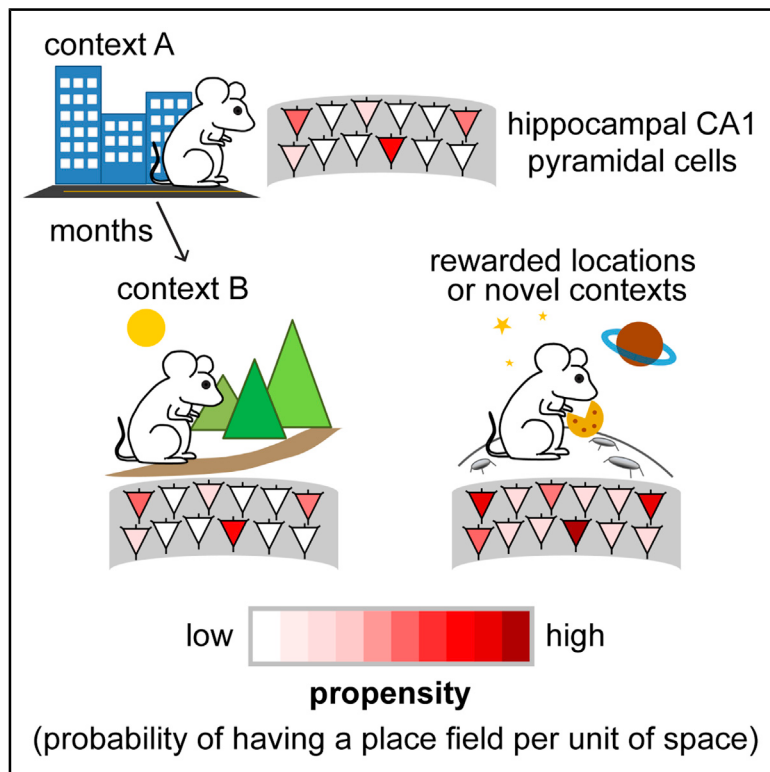


The Statistical Structure of the Hippocampal Code for Space as a Function of Time, Context, and Value

Graphical Abstract



Authors

Jae Sung Lee, John J. Briguglio,
Jeremy D. Cohen, Sandro Romani,
Albert K. Lee

Correspondence

leej13@janelia.hhmi.org (J.S.L.),
briguglioj@janelia.hhmi.org (J.J.B.),
sandro.romani@gmail.com (S.R.),
leea@janelia.hhmi.org (A.K.L.)

In Brief

A unified response pattern of hippocampal place cells, driven by individual cell-intrinsic mechanisms, quantitatively predicts the structure of representation of space at the population level across varying conditions by the hippocampus in mice.

Highlights

- Each CA1 pyramidal neuron has a propensity to have place fields that differs across cells
- A cell's propensity is fixed across contexts and time, scaled in rewarded and novel areas
- The subpopulation of low propensity cells yields a sparse code for location
- Intracellular data provide evidence that excitability underlies propensity differences



Article

The Statistical Structure of the Hippocampal Code for Space as a Function of Time, Context, and Value

Jae Sung Lee,^{1,*} John J. Briguglio,^{1,*} Jeremy D. Cohen,¹ Sandro Romani,^{1,*} and Albert K. Lee^{1,2,*}

¹HHMI Janelia Research Campus, Ashburn, VA, USA

²Lead Contact

*Correspondence: leej13@janelia.hhmi.org (J.S.L.), briguglioj@janelia.hhmi.org (J.J.B.), sandro.romani@gmail.com (S.R.), leea@janelia.hhmi.org (A.K.L.)

<https://doi.org/10.1016/j.cell.2020.09.024>

SUMMARY

Hippocampal activity represents many behaviorally important variables, including context, an animal's location within a given environmental context, time, and reward. Using longitudinal calcium imaging in mice, multiple large virtual environments, and differing reward contingencies, we derived a unified probabilistic model of CA1 representations centered on a single feature—the field propensity. Each cell's propensity governs how many place fields it has per unit space, predicts its reward-related activity, and is preserved across distinct environments and over months. Propensity is broadly distributed—with many low, and some very high, propensity cells—and thus strongly shapes hippocampal representations. This results in a range of spatial codes, from sparse to dense. Propensity varied ~10-fold between adjacent cells in salt-and-pepper fashion, indicating substantial functional differences within a presumed cell type. Intracellular recordings linked propensity to cell excitability. The stability of each cell's propensity across conditions suggests this fundamental property has anatomical, transcriptional, and/or developmental origins.

INTRODUCTION

How the brain represents the world is a central question in neuroscience. Representations in many primary sensory areas display localized receptive fields organized topographically (Penfield and Boldrey, 1937; Talbot and Marshall, 1941; Mountcastle, 1957; Hubel and Wiesel, 1962). In the hippocampus, an animal's location in a given environment (context) is represented by place cells and their spatial receptive fields (place fields) (O'Keefe and Dostrovsky, 1971). Unlike primary visual or somatosensory areas, however, hippocampal place cell representations are not topographically organized (e.g., nearby cells have fields that are far apart) (O'Keefe, 1976). Furthermore, individual place cells can have multiple fields in an environment (O'Keefe, 1976; Fenton et al., 2008; Rich et al., 2014), fields of multi-field cells are randomly dispersed across the environment (Rich et al., 2014), cells shuffle their field locations when in a different environment (O'Keefe and Conway, 1978; Muller and Kubie, 1987; Leutgeb et al., 2005), and cells may have no fields (be "silent") in some environments (O'Keefe and Conway, 1978; Thompson and Best, 1989; Wilson and McNaughton, 1993; Epsztain et al., 2011; Alme et al., 2014; Rich et al., 2014). Therefore, hippocampal representations possess several features that appear random—something that is shared by association areas and other regions (Rigotti et al., 2013).

Hippocampal representations also exhibit clearly nonrandom structure. In particular, use of large environments revealed fields are not distributed randomly across the population, which would yield a Poisson distribution of field numbers per neuron (Figure 1A, "equal Poisson"). Instead, the propensity of a hippocampal CA1 neuron (i.e., its probability of having a place field per unit of space) varies greatly across cells. Specifically, the distribution of propensities follows a highly skewed gamma distribution (Figure 1A) such that many cells have a low propensity, some have high propensity and others have in-between values (Rich et al., 2014). Furthermore, given its propensity, a cell's fields are distributed randomly in space (spatial Poisson) (Rich et al., 2014). Thus, fields are distributed across the population according to a gamma-Poisson distribution—for each cell, its propensity value is drawn from a gamma distribution, then its fields occur in the environment as a spatial Poisson process with rate equal to the cell's propensity. Similarly skewed distributions have been found in other hippocampal regions (Alme et al., 2014; Witharana et al., 2016) and the olfactory system (Turner et al., 2008), suggesting this may be a general property (Buzsáki and Mizuseki, 2014) of representations across many brain areas (where propensity would be the probability a cell participates in the representation for each item of concern).

A potential function of a highly skewed distribution of field propensity is that the many low propensity cells result in a sparse



code for location (e.g., a substantial fraction of cells have exactly one place field across a large extent of space). Sparse coding has desirable properties, including simple mechanisms for readout and forming associations, and increased memory storage and retrieval capacity (Tsodyks and Feigelman, 1988; Olshausen and Field, 2004; Katkov et al., 2017). However, for sparse coding to work in this way, the same cells would need to have low propensity across different environments and over time (Figure 1B), which has not been shown. More generally, if each cell's propensity were preserved across different conditions, this would indicate a significant degree of structure underlying all hippocampal representations.

Separately, hippocampal representations are influenced by sensory and value cues. CA1 place field density is elevated in consistently rewarded locations (Hollup et al., 2001; Dupret et al., 2010; Danielson et al., 2016; Zaremba et al., 2017; Gauthier and Tank, 2018; Sato et al., 2018). In previous work on propensity, value was spatially homogeneous across the environment (Rich et al., 2014; Alme et al., 2014; Witharana et al., 2016). How do value-based modulations in overall field density relate to each cell's propensity? If a cell's reward activity was correlated with its field propensity, this would yield a sparse code for all locations, including rewarded ones (Figure 1C). This in turn could support the hippocampus' role in navigation to spatial goals (Morris et al., 1982).

Here, we bring together these features of hippocampal CA1 representations to develop a unified statistical description of place field structure with respect to time, context, and value. We employed two-photon calcium imaging of the hippocampus in awake head-fixed mice (Dombeck et al., 2010; Lovett-Barron et al., 2014; Sheffield and Dombeck, 2015; Basu et al., 2016; Danielson et al., 2016; Malvache et al., 2016; Gauthier and Tank, 2018; Hainmueller and Bartos, 2018; Sato et al., 2018) as they navigated multiple large virtual environments. Large environments (Kjelstrup et al., 2008) allowed high-resolution measurement of field statistics such as propensity (Fenton et al., 2008; Rich et al., 2014) and virtual reality enabled use of many large environmental contexts. Imaging also allowed propensities of large numbers of individual cells to be tracked for months (Ziv et al., 2013; Rubin et al., 2015). This allowed us to test whether propensity is preserved across environments and time. Finally, by manipulating reward contingencies in these environments, we investigated the interaction of value and propensity. The result of our work is a simple probabilistic model centered on the field propensity that predicts the structure of hippocampal representations under a wide variety of conditions. In particular, we found that propensity is highly preserved across conditions including reward (via multiplicative scaling), thus simultaneously yielding a sparse code for all locations and a dense code among distinct sets of cells.

RESULTS

Long-Term Calcium Imaging in Multiple Large Virtual Environments

Mice ran on a 40-cm spherical treadmill at the center of a half-cylindrical screen on which monochromatic virtual environments were projected (Figure 1D) (Harvey et al., 2009; Dombeck

et al., 2010; Cohen et al., 2017). The animal's view of an environment was updated based on treadmill movement. We designed 4 different environments with distinctly shaped ~40 m-long tracks surrounded by unique objects (Figures 1D and S1). Each animal explored 3 environments (A, B, and C; A represents the first one explored regardless of identity; Figure 1E), each accompanied by a distinct odor cue. Animals ran the full track length in one direction then were teleported to the start for another run, for 4–8 runs total per environment (session). Animals explored each environment over multiple days. All analyses were performed on sessions where the environment was familiar (≥ 4 days of previous experience), unless otherwise noted. In the first set of experiments, water reward was provided at random locations that changed on each run. We imaged the calcium activity of dorsal hippocampal CA1 pyramidal neurons in transgenic mice ($n = 4$) expressing GCaMP6f (Dana et al., 2014); 700–870 neurons were identified per session, and we could follow 125–430 neurons across all sessions for up to 3 months (Figure 1F).

Field Propensity Varies Greatly across Cells

For the first element of the model, we quantified the distribution of the number of place fields per neuron. In agreement with Rich et al. (2014), the field number distribution across the population was highly skewed, well-fit by a gamma-Poisson distribution, and far more spread out than predicted by a (equal-)Poisson distribution (Figures 1G and S2), which would be expected if each cell had the same propensity to have a place field per unit space. Therefore, different cells have clearly different field propensities. Furthermore, given its propensity, each cell's fields were distributed randomly in space (spatial Poisson per cell, Figure S2 legend). Several features of fields (e.g., width) were similar for low and high propensity cells (Figures S1D–S1F). These calcium imaging results in head-fixed mice exploring familiar virtual environments thus match those from extracellular recordings in freely moving rats running on a novel 48 m track (Rich et al., 2014). Moreover, the skewed field number distribution was unchanged by time or environmental context (Figures 1H and S2, Kolmogorov-Smirnov [K-S] test, $p > 0.15$) and not explained by the change in mean field number along proximal-distal (HenrikSEN et al., 2010) or superficial-deep (Mizuseki et al., 2011) axes (Figure S3A).

Individual Cells Preserve Their Field Propensity over Time

Cells show different propensities, but is each cell's propensity preserved over time? First, we checked the stability of field locations in each environment. As seen in freely moving animals exploring small (~1 m) environments (Mankin et al., 2012, 2015; Ziv et al., 2013; Rubin et al., 2015), CA1 fields represented the same location for ~2 weeks but gradually changed over time. This was quantified using field center location, the correlation between population vectors (PVs) of the simultaneous activity pattern across all cells at corresponding locations, and Bayesian decoding of location (Davidson et al., 2009) (Figures 2A–2D; statistical significance is reported in figures if not in text).

Although field locations changed such that decoding performance decreased to chance after ~2 weeks, surprisingly each

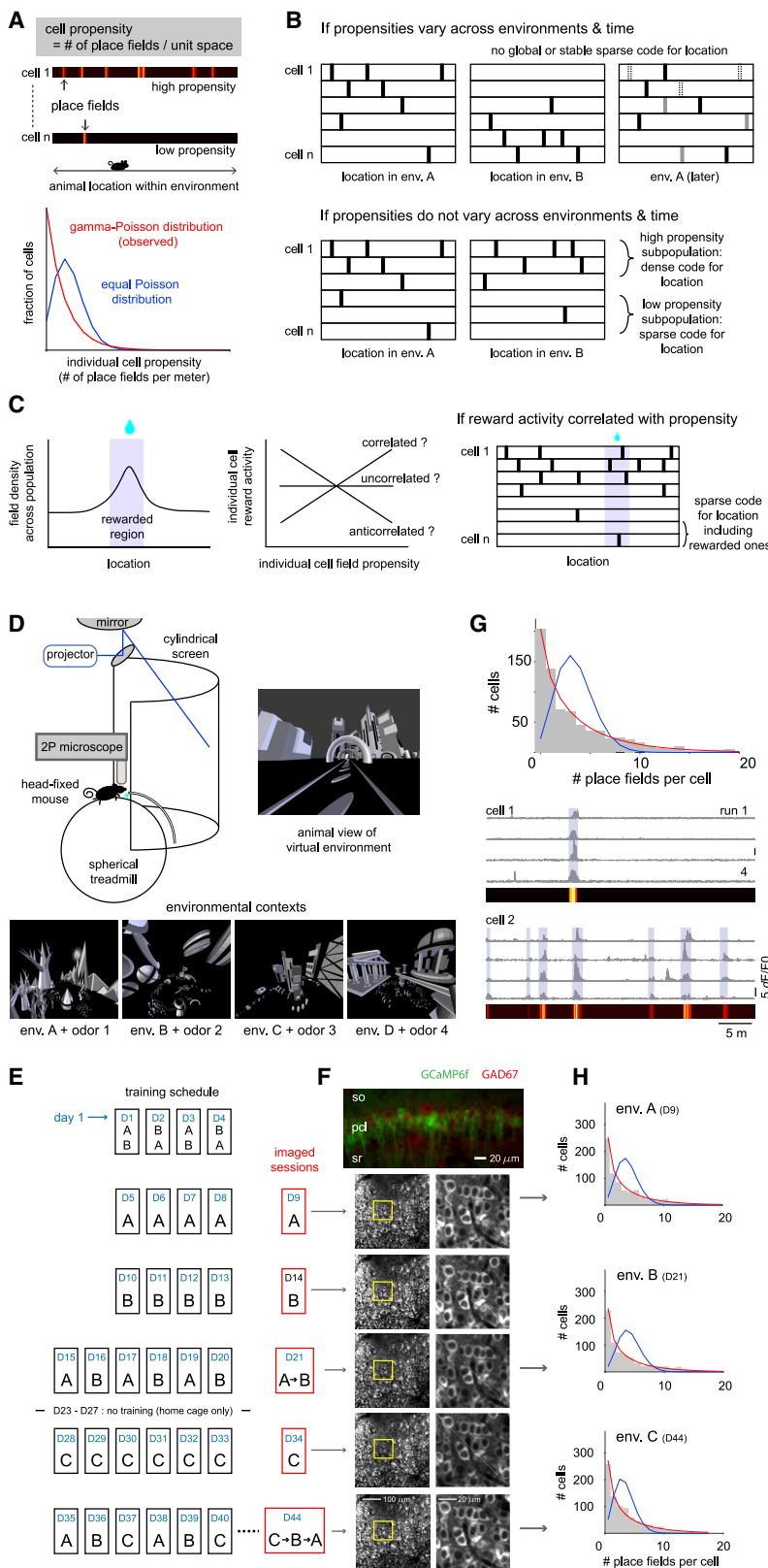


Figure 1. Skewed Distribution of Place Field Propensity of Hippocampal CA1 Pyramidal Cells in Multiple Large Virtual Environmental Contexts Observed with Longitudinal Two-Photon Calcium Imaging

(A) Number of place fields per cell assuming cells have same (equal Poisson, blue) or gamma-distributed Poisson (observed, red) rate of forming place fields per unit length.

(B) Preservation of each cell's propensity across environments and time would yield a sparse code for location (black, place fields; gray, new fields; open boxes, fields that disappeared).

(C) Schematic of known increase in field density in consistently rewarded locations (left). Possible relationship between propensity and reward activity (middle). Correlation between reward activity and non-reward field propensity would yield a sparse code for all locations, rewarded and non-rewarded (right).

(D) Experimental apparatus and large virtual environments (bottom).

(E) Training and imaging schedule in 3 different environments: day 1 (D1) to 44.

(F) Top: GCaMP6f-expressing cells (green) do not express GAD67 (red). Standard deviation images of GCaMP6f traces in run 1 (left column). Imaging sessions indicated by arrows from (E). Close up of yellow boxes (right column).

(G) Place field number distribution in an environment (top). Fit of equal-Poisson (blue) or gamma-Poisson (red) distribution. Example place cells with 1 (middle) and 7 fields (bottom). Activity in each of 4 runs across environment above and average activity below.

(H) Field number distribution in 3 different environments on different days.

See also Figures S1, S2, and S3.

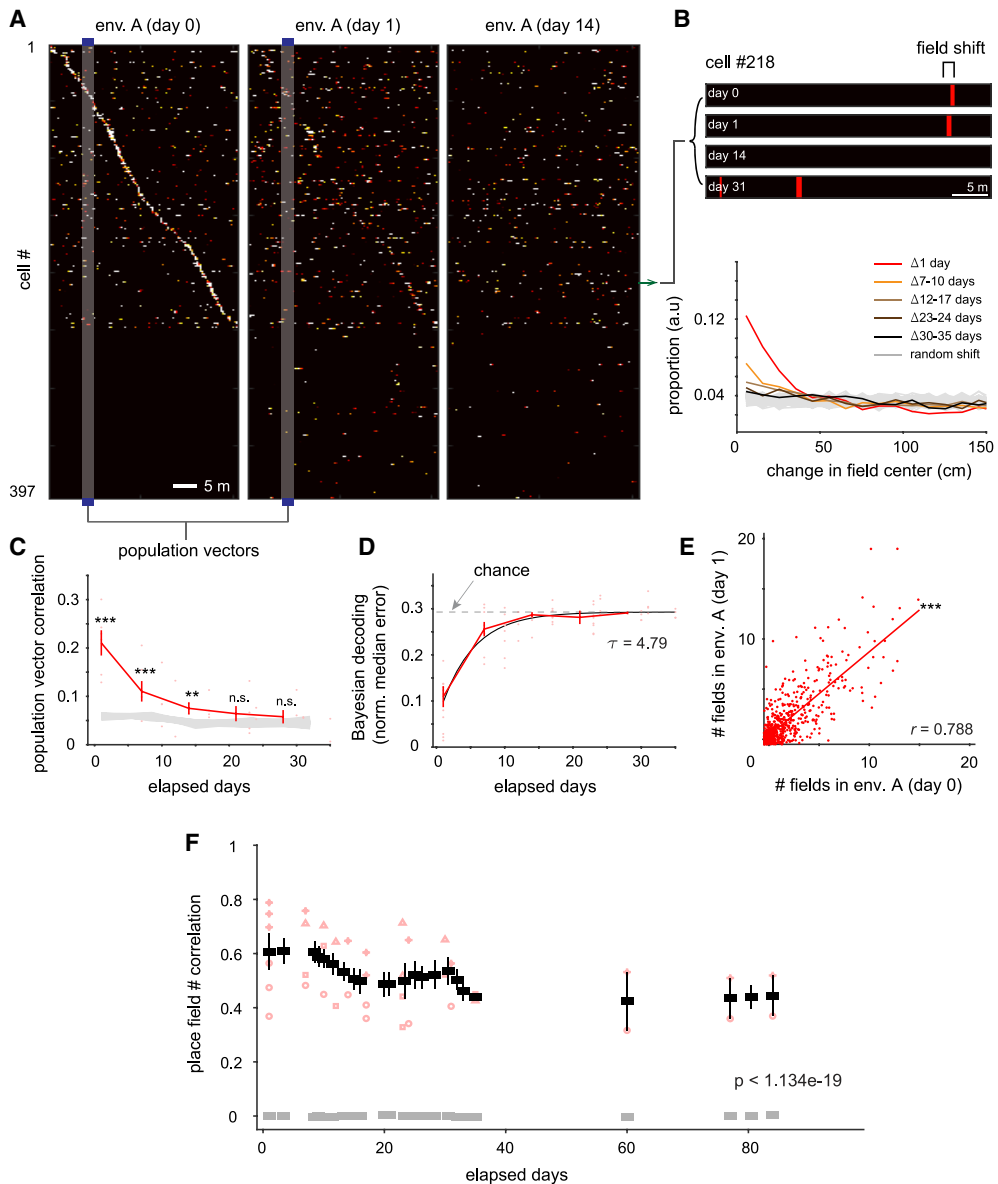


Figure 2. Field Propensity of Each Cell Is Preserved over Time in the Same Environmental Context, Even while the Place Field Representation of that Environment Gradually Evolves

(A) Each cell's calcium activity in runs 1–4 were averaged on each day. Cells ordered by location of peak activity on day 0. Same order was kept for days 1 and 14.
 (B) Example cell's field shifts in same environment over time (top). Shift of field centers pooled over all pairs of sessions and animals (23,417–38,063 field pairs for each group of days, bottom). Data from mouse 1 and 2 days 8 and 22 were added for Δ1 day results here and Figures 2C, 2D, 4A, and 4B.
 (C) Average correlation between binary place field population vectors for same location in same environment on different days (mean ± SEM, 4 mice; gray, shuffled data; elapsed day range groups: 1, 4–10, 11–17, 18–24, ≥25, also in (D); small red marks, individual session pairs).
 (D) Normalized median error (fraction of entire environment) of Bayesian decoding of animal location on 1 day based on activity from a different day.
 (E) Each point (jittered) shows one cell's place field numbers on 2 different days in the same environment.
 (F) Correlation of number of fields per cell across pairs of sessions in same environment (e.g., correlation of points in E; red, individual session pairs, unique symbol per mouse; black, mean ± SEM of individual values centered on that day ± 5 days; gray, mean ± SEM of 100 shuffles of data, ± 5 days; mean ± SEM shown once for windows consisting of same set of values; p value is least significant p value of all window comparisons to corresponding shuffles; same scheme used in Figures 3F, 4A, 4B, and 4E). In all figures: n.s.: not significant ($p > 0.05$); * $p < 0.05$; ** $p < 0.01$; *** $p < 0.001$.

cell's field propensity was preserved across months in an environment. Specifically, the Pearson correlation of each cell's field number on different days (Figure 2E) was significantly above chance for intervals up to at least 2.5 months (Figure 2F).

Individual Cells Preserve Their Field Propensity across Distinct Environmental Contexts

We next tested whether environmental context affects each cell's propensity. We first checked if place field representations

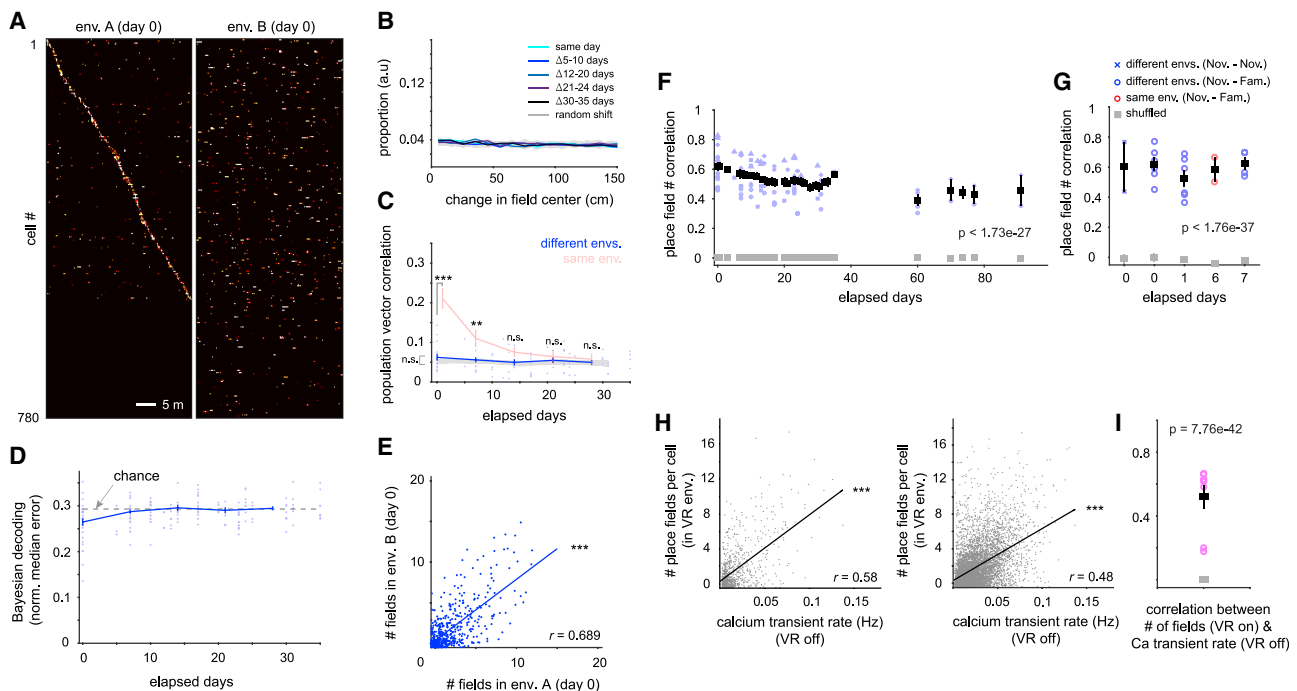


Figure 3. Field Propensity of Each Cell Is Preserved across Distinct Environmental Contexts, Even though Place Field Representations Are Completely Different

(A–F) Similar to Figures 2A–2F except for different environmental contexts (elapsed day range groups in C; D: 0, 4–10, 11–17, 18–24, ≥ 25). Result for different environments in (C) was similar when population vectors were compared between locations in one environment with circularly shifted locations in the other.

(G) Field number correlation between environments where one or both are novel (mean \pm SEM).

(H) Calcium transient rate in dark and subsequent session field number per cell (example session, left; 2 sessions each from 4 mice pooled, right).

(I) Correlation as in (H), left, (circles, 8 sessions, 2 each from 4 mice; black, mean \pm SEM; gray, shuffle).

in different large environments were distinct (global remapping) (O'Keefe and Conway, 1978; Muller and Kubie, 1987; Leutgeb et al., 2005), as in standard-sized ($\sim 2\text{--}4$ m) virtual environments (Danielson et al., 2016; Cohen et al., 2017; Gauthier and Tank, 2018). In contrast to the similarity of field locations in an environment over time, representations of different environments were uncorrelated as assessed by the same measures (Figures 3A–3D).

Although place codes were distinct across environments, each cell had similar numbers of fields in all contexts for as long as we performed experiments (up to 90 days) (Figures 3E and 3F), including environments explored for the first time (Figure 3G). Preservation of propensity across environments is surprising as fields can be controlled by sensory inputs (O'Keefe and Conway, 1978; Muller and Kubie, 1987; Deshmukh and Knierim, 2013; Geiller et al., 2017), and the environments were visually very different. To explore this further, for some sessions we placed animals on the treadmill in the dark with no odor cue before turning on the virtual environment. Each cell's "dark" activity level was correlated with its field propensity (Figures 3H and 3I), suggesting preservation of propensity did not depend on low-level similarities in visual features between environments.

As propensity was preserved, we combined field numbers of each cell across environments and sessions to give the highest resolution measure of propensity. The resulting propensities

within an animal ranged over an order of magnitude (gamma fit 90:10 percentile propensity ratio mean: $24.4 \times$, range: $6.1\text{--}48.0 \times$; versus equal-Poisson fit mean: $1.9 \times$, range: $1.7\text{--}2.2 \times$; 4 mice, Figures S3B–S3D). A simple model with a fixed propensity per cell could explain 66% of the observed variance in fields per cell across sessions (see STAR Methods).

The time course of the field number correlation was similar for same and different environments (Figure 4A). The mean calcium transient rate per cell in a session, irrespective of where transients occurred, was also highly correlated across sessions and followed a similar time course (Figure 4B) (note a cell's transient and field numbers were highly correlated within a session: $r = 0.88 \pm 0.01$, mean \pm SEM, 34 sessions). Together, these results suggest that the overall excitability of each CA1 neuron is the determining factor for field propensity.

Propensity Is Preserved across Long Time Periods without Task Experience

Experiments in smaller environments showed hippocampal activity in a session makes activity in the next session more likely, but not if the gap is ≥ 1 day (Cai et al., 2016). Therefore, we tested if the persistent field number correlation in large environments required daily virtual environment experience in the intervening period. Animals were kept in their home cage for 5- or 60-day periods without virtual environment exposure. Propensity was highly correlated even across a 2-month gap. The

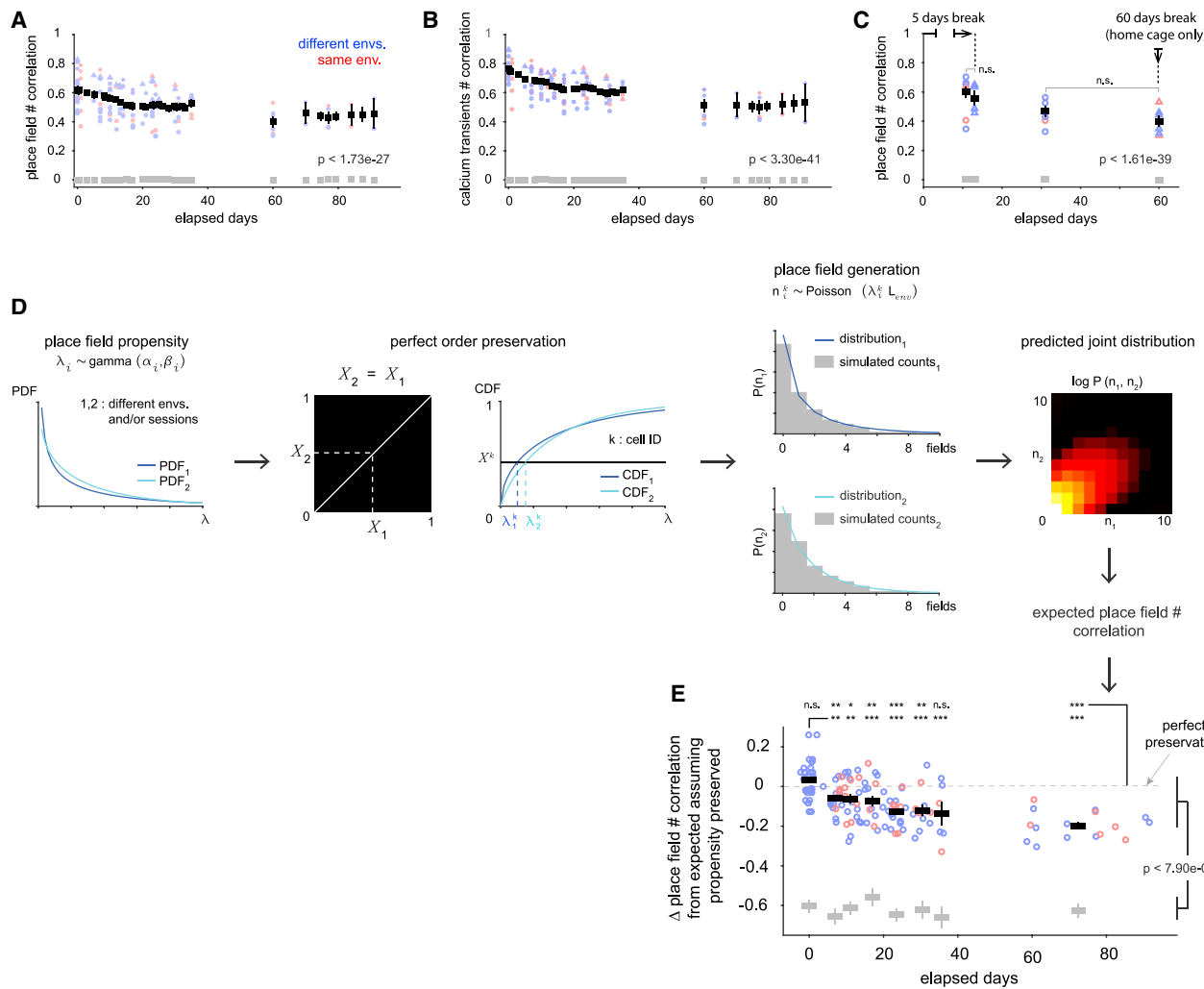


Figure 4. Propensity of Each Cell Is Highly Preserved across Days and Environments

(A) Place field number correlation in same (Figure 2F) or different (Figure 3F) environments combined.

(B) Same as (A) except calcium transient number correlation.

(C) Field number correlation between sessions with intervening gap of 5 or 60 days limited to home cage. Values without gap in training (to left).

(D) Model for computing expected field number correlations in (A) assuming each cell's (relative) propensity was perfectly preserved across sessions. Propensities were drawn from gamma distributions (fit to each session) and modeled as order-preserving (i.e., each cell sits in same place in the CDFs across sessions). Each cell's field number was modeled as a Poisson variable based on its propensity in each session, giving a joint distribution of field numbers per cell across sessions, from which expected correlations were computed.

(E) Difference between observed field number correlation and expected correlation assuming perfect order preservation of propensity. Each group's correlations were compared to 0 (perfect preservation) (top), 0 elapsed days (middle), shuffle (bottom). Points jittered in x.

correlation across a given gap was the same whether it contained a 5-day home cage-only period or not (Figure 4C).

Time Course of Preservation of Field Propensity

We developed a statistical model to further investigate the time course of propensity. Field number correlations decayed from ~ 0.6 for short time gaps to ~ 0.4 beyond a month (Figure 4A). Because field occurrence is well-modeled as a spatial Poisson process (Rich et al., 2014), the same underlying propensity is expected to produce varying numbers of fields per session, at least for distinct environments. Thus, correlations are expected to be <1 even if propensities were perfectly preserved. Additionally,

the gamma propensity distribution exhibited some session-to-session variation (Figure 4D), which would also lower correlations even if the ordering of each cell's propensity in the population was perfectly preserved. We created a model that took these factors into account by fitting a gamma distribution to each session, assuming the ordering of each cell's propensity was perfectly preserved across sessions, then computing the expected field number correlation (Figure 4D). The observed minus expected correlations measure how close the data was to perfect preservation of (relative) propensities (Figure 4E). For different environments explored on the same day, correlations matched perfect preservation. Although correlations gradually

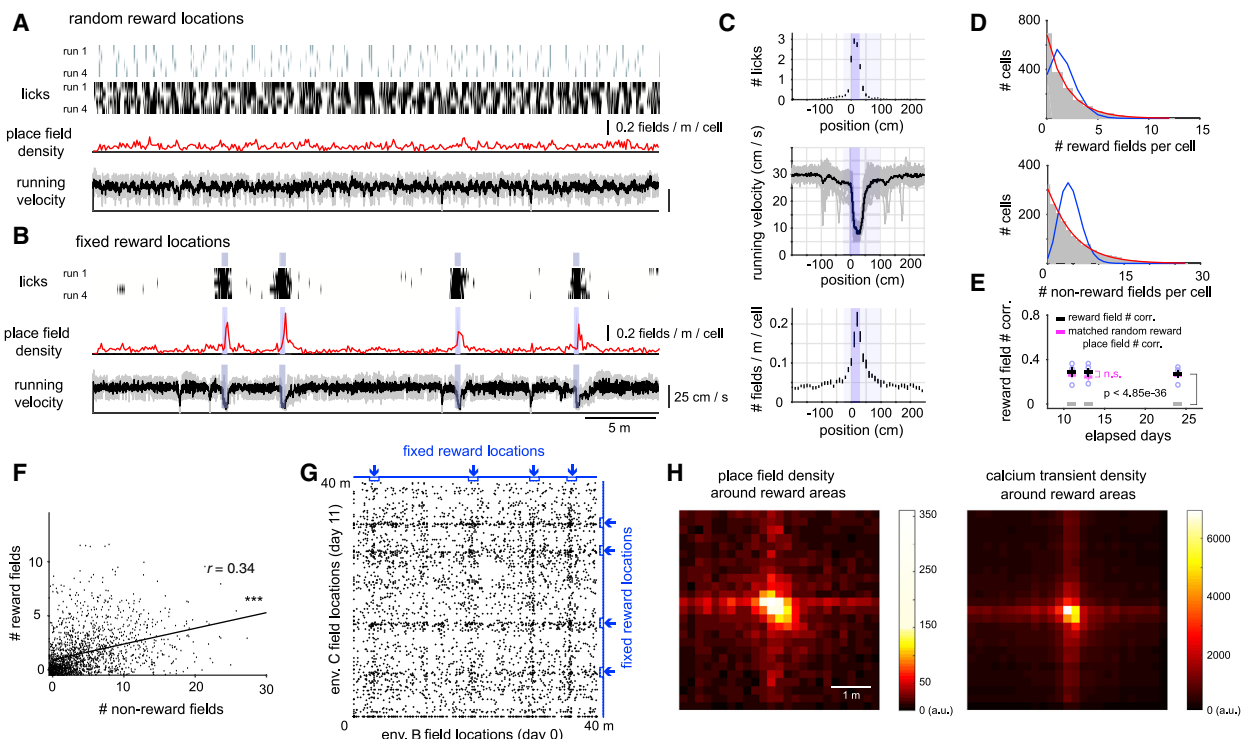


Figure 5. Hippocampal Reward-Related Activity of Each Cell Is Correlated with Its Non-reward Place Field Propensity

(A) Water reward (blue) and lick (black) locations, place field density, and running speed (gray, each run, black, average) in random reward sessions (Figures 1, 2, 3, and 4).

(B) Same as (A) for sessions where reward provided at 4 fixed locations in each run.

(C) Licks, speed, and field density around fixed reward locations (average of 4 reward locations per session, 3 sessions per animal). Blue, location where reward delivered; light blue, region of elevated field density defined as reward area in subsequent analysis.

(D) Reward and non-reward field number per cell distributions. Equal Poisson (blue) and gamma-Poisson (red) fits. Field numbers combined over 3 fixed reward sessions, 4 mice.

(E) Reward field number correlations (black; blue, session pairs) across 3 distinct fixed reward environments (gray, shuffle). Values were similar to field number correlations (pink) for subsections (25% of total length) of random reward environments matched to have same mean field number (0.51–0.52) per session ($p = 0.49$ –0.83 for 3 matched time gaps).

(F) Reward and non-reward field number (combined over 3 sessions) per cell (4 mice).

(G) Field locations of individual cells in pair of fixed reward (blue arrows) environment sessions (one point for every possible pair of session 1 and session 2 fields of each cell). See text.

(H) Field or calcium transient pair density around fixed reward areas (20-cm bins), summed over all pairs of fixed reward locations (e.g., 16 intersection points in G) in all fixed reward session pairs.

See also Figure S4.

decreased below perfect preservation over a month, overall this analysis revealed each cell's propensity was highly preserved across environments and time.

Increased Place Field Density at Rewarded Locations

Salient stimuli, such as reward, influence hippocampal representations, so we performed additional experiments to incorporate this key feature into our model. We altered reward contingencies to investigate the relationship between reward-related activity and place field propensity. In the experiments above and the previous study of propensity in large environments (Rich et al., 2014), reward was delivered at random locations differing in each run (Figure 5A). CA1 field density across the population is ~2–3× higher in consistently rewarded locations (Hollup et al., 2001; Dupret et al., 2010; Danielson et al., 2016; Zaremba

et al., 2017; Gauthier and Tank, 2018; Sato et al., 2018), thus propensity increases for at least some neurons relative to non-rewarded regions. Is the increase concentrated in a small subset of cells that specifically respond to reward (Gauthier and Tank, 2018; Sato et al., 2018), or spread across the population and, if so, in what manner (Figure 1C)? If a cell's reward activity was un- or anticorrelated with its propensity in non-rewarded regions, there would be no sparse coding overall, because no cells would be low propensity across all locations, rewarded and not.

We delivered reward at 4 locations in each run while matching the total reward per run given in the random reward sessions. We presented 3 distinct sets of 4 fixed reward locations (1 set in environment B, 2 in C) per animal (Figure S4A). For each set, we analyzed the last session after animals were exclusively trained with that set for ≥5 days in a row. Animals learned these high

value locations—lick rate increased and running speed decreased predictively before each reward location (Figures 5B and 5C). We observed the reported ~2–3× increase in field density around reward locations (Figures 5B and 5C). Average field density was elevated ~25 cm before to ~75 cm after each 25 cm-wide rewarded region (Figure 5C), which we used as the reward areas (125 cm each for 4 areas) in our analysis. The field density increase in rewarded areas was 2.62 ± 0.15 (range: 2.14–3.78, 12 sessions) times the 0.0393 ± 0.0025 fields/m²/cell in non-rewarded areas (similar to the 0.0447 ± 0.0025 fields/m²/cell in random reward sessions, $p = 0.37$). This increase could not be attributed to decreased running speed around reward areas, as calcium activity generally increased with speed in non-rewarded areas (transient number-speed correlation, 25 cm spatial bins: 0.14–0.34, 12 sessions).

Reward Field Propensity Is Highly Skewed and Preserved across Distinct Environmental Contexts and Time

We asked if cells differed in the probability of representing rewarded locations. To increase sampling, we merged the number of reward fields (i.e., place fields in reward areas) per cell across the 3 distinct fixed reward sessions. The reward field number distribution was skewed; most cells had few or 0 reward fields (Figure 5D). The non-reward field (place fields outside reward areas) number distribution was also skewed to 0 (Figure 5D). Both distributions were better fit by a gamma-Poisson than Poisson distribution.

As with field propensity, each cell displayed a similar number of reward fields across different environments and time (Figure 5E). Non-reward field number correlations did not differ from random reward condition values ($p = 0.36$ –0.74, Figure S4B). Reward field number correlations were lower than for non-reward fields but similar when controlling for the lower reward field numbers (Figure 5E).

Reward Field Propensity Is Correlated with Field Propensity

Because both field and reward field propensity were skewed and stable across environments and time, we investigated the cell-by-cell relationship between these propensities. Do cells with higher field propensity also respond more at rewarded locations? Is there a subset of cells (~5%) specialized for representing reward (Gauthier and Tank, 2018; Sato et al., 2018)? For this analysis, we combined reward and, separately, non-reward field numbers of each cell across the 3 distinct fixed reward sessions and pooled over animals.

Reward and non-reward field numbers of neurons were correlated (Figure 5F) ($r = 0.34$, $p = 7.7e-48$, 1,735 cells tracked across all 3 sessions; mouse 1–4: 522, 451, 616, and 146 cells, respectively).

Next, we looked for a class of reward-specific neurons. Most cells (90.3%) with a reward field also had non-reward fields. None had 12 reward fields (a field at every reward location) and 0 non-reward fields; only 1 cell had 12 reward fields, and it also had 8 non-reward fields. The 5% of cells with the most reward fields had many non-reward fields (Figure S4D). 5.8% of cells had ≥ 1 reward field and 0 non-reward fields, and these

cells mostly had 1 reward field out of 12 possible (Figure S4E). Only 1 cell exhibited context-specific reward-specific activity (Figure S4F). These results suggest reward activity represents a conjunction of reward \times place, rather than reward per se.

Which cells contributed to increased field density at reward locations? For each pair of fixed reward sessions, we created a plot with a point at (x,y) whenever a neuron had a (reward or non-reward) field at location x in session 1, and y in session 2 (Figure 5G) (Gauthier and Tank, 2018; Sato et al., 2018). Cells with n and m fields in sessions 1 and 2 contributed nm points. (If a cell had 0 fields in a session, point(s) were placed at 0 for that session.) The increased density of points along vertical and horizontal lines at reward locations indicated that cells contributing to the excess reward field density (over the non-reward density) also had non-reward fields (Figure 5G). This was also seen in the average of such plots centered on every point corresponding to a reward location in both sessions (Figure 5H). That is, excess reward field density did not exclusively emerge from cells that only had reward fields. The result was the same considering all calcium transients whether inside or outside of fields (Figure 5H).

Reward Multiplies Each Cell's Field Propensity by a Constant Gain Factor

Because we discovered reward and non-reward field propensities are correlated, we examined statistical models of the joint distribution of reward and non-reward fields of individual cells across the population. The simplest model giving correlated reward and non-reward field numbers is a “constant gain” model, where reward field propensity equals a common gain value times the non-reward field propensity. The joint distribution was well-accounted for by the perfectly correlated (i.e., perfect order preserving) constant gain model in 2 of 4 animals (Figure 6A, right). We expanded the constant gain model using a Clayton copula to generate correlated (but not perfectly scaled) reward and non-reward propensities (Figure 6A). The copula guarantees the separate (marginal) reward and non-reward field number distributions are preserved while allowing variation between perfectly correlated and completely uncorrelated reward and non-reward propensities with a single continuous correlation parameter (1 = perfect scaling, 0 = uncorrelated). The copula allows a cell with non-reward propensity λ_i to have a reward propensity near $G\lambda_i$ instead of constraining it to equal $G\lambda_i$, where G is the overall gain. The copula parameter was fit to the reward and non-reward field number correlation (not to the full joint distribution). The fit was assessed by estimating the similarity (Jensen-Shannon divergence, D_{JS}) between the resulting model and full joint distribution of reward and non-reward field numbers. For all animals, the copula models fit the data with high correlation (mean: 0.75) between reward and non-reward propensities (Figure 6B) (fit gains: 2.94 ± 0.20 , range: 2.19–4.20, 12 sessions). We tested alternative models in which gain could vary nonlinearly but monotonically with the non-reward propensity. Copula models were better (lower D_{JS}) than these models that notably had more (5 versus 4) parameters and were fit to the full joint distribution (Figure 6C). Thus, the hippocampal representation of value is well-described as a uniform value-driven scaling of each cell's underlying place field propensity. This tight correlation of reward

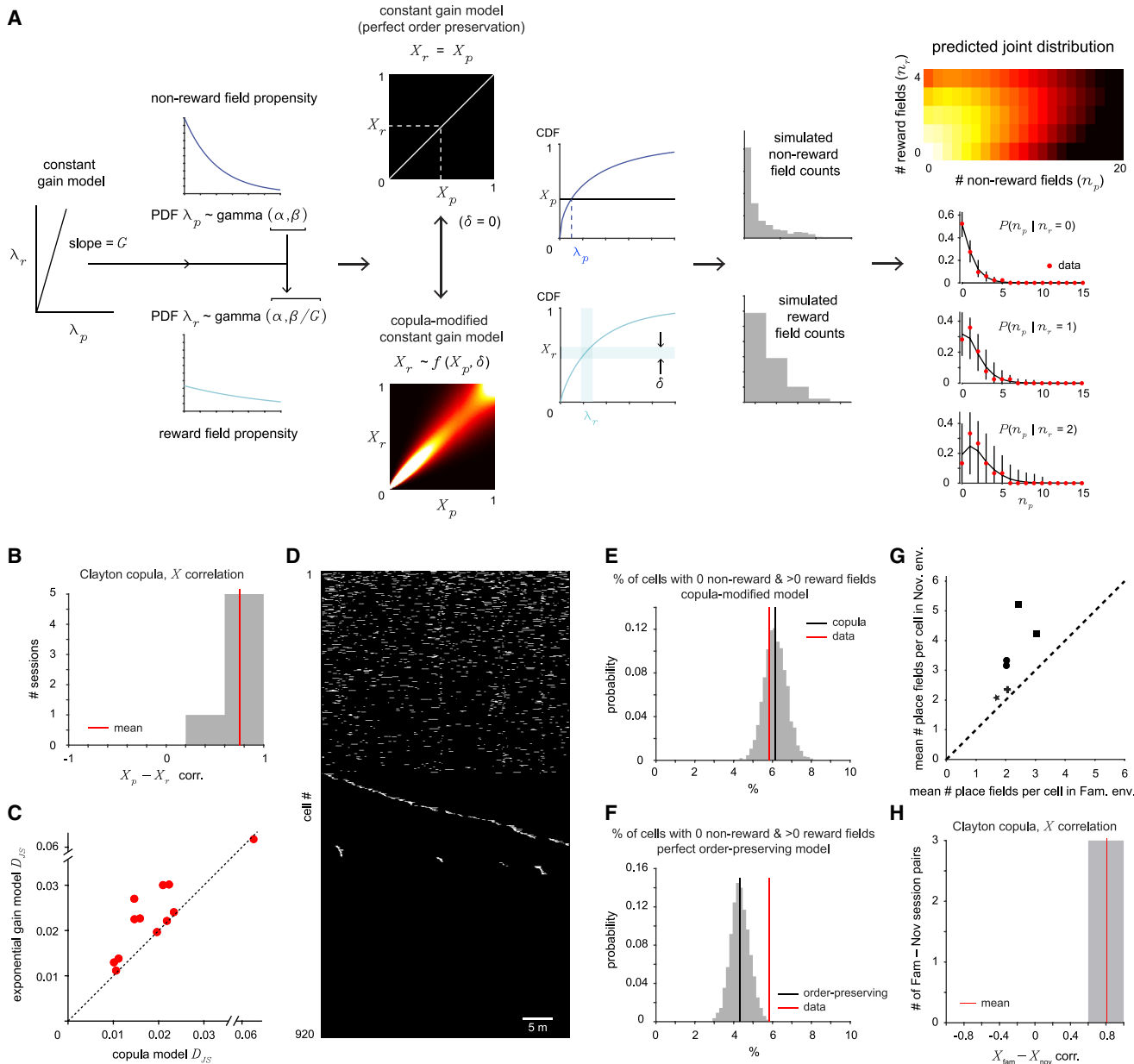


Figure 6. Reward-Related Activity Is Proportional to Non-reward Field Propensity

- (A) To model reward activity, we assumed the distribution of reward propensities across cells had a constant gain with respect to the non-reward field propensity, yielding a scaled gamma distribution. We tested models with perfect order preservation (each cell's reward propensity = a constant \times its non-reward field propensity) and parameterized correlated activity (copula), where reward and non-reward field numbers are determined by Poisson processes with rates given by the respective propensities. This yields joint distributions of reward and non-reward field numbers per cell that are compared to data.
- (B) Correlations of copula models fit to each fixed reward session ($n = 12$) were very high for most sessions (1 implies perfect order preservation).
- (C) Performance of copula model and a parameterized gain model in predicting actual joint distribution for each fixed reward session shows consistently better agreement (lower D_{JS}) of copula model. See text.
- (D) Example session. Cells ordered by number of fields. Cells with 1 field total (non-reward or reward) in environment ordered by location (separately for non-rewarded, rewarded areas).
- (E) Distribution of proportion of “reward only” cells predicted by copula model. Observed number of reward-only cells is well-predicted by copula model.
- (F) Same as (E) but for order-preserving model. Most of observed cells are accounted for by perfect order-preserving model.
- (G) Mean field number per cell in first (novel) session in an environment and in a session when it was very familiar (≥ 15 previous sessions in that environment, 6 random reward session pairs, unique symbol per mouse).
- (H) Correlations of copula models fit to each novel-familiar pair ($n = 6$) show the increased activity in novel over familiar environments is also well-predicted by copula model.

See also Figure S5.

activity and non-reward field propensity results in a sparse code for all locations, rewarded and not, among the low propensity cells—e.g. Figure 6D shows many cells with 1 reward field (of 4 possible ones) and 0 non-reward fields in an environment.

Using the copula model, we revisited the issue of reward-specific cells. The copula model's predicted distribution of cells with ≥ 1 reward field and 0 non-reward fields, i.e., candidate reward-specific cells could explain all 5.8% of cells observed to have ≥ 1 reward field and 0 non-reward fields (Figure 6E). The perfect order preserving model could account for most (median: 4.3%, 95% confidence interval [CI]: 3.4%–5.3%, Figure 6F). Both models assume no reward-specific subpopulation.

Novelty Multiplies Each Cell's Field Propensity by a Constant Gain Factor

Like reward, novelty strongly modulates CA1 activity. CA1 pyramidal cells display elevated firing rates in novel versus familiar environments (Nitz and McNaughton, 2004; Karlsson and Frank, 2008; Cohen et al., 2017). Field numbers per cell were highly correlated between novel and familiar environments (Figure 3G). Can the constant gain-copula model also explain the increased overall activity in novel environments? We analyzed all 6 pairs of random reward sessions where one session was the novel experience, and the other a very familiar experience, in an environment. Overall calcium and field activity was lower in familiar environments (Figures 6G and S5A), consistent with previous spike recordings. The copula model fit the data (mean correlation: 0.81, Figure 6H) as well as for reward, implying each cell's propensity is scaled up by a constant factor in novel versus familiar sessions. Thus, an overall gain in propensities may be a general phenomenon for understanding how the hippocampus responds under a range of conditions.

Propensity Is Anatomically Distributed in Salt-and-Pepper Fashion

As each cell's propensity was preserved under all conditions tested, we looked for an anatomical organization of propensity (Figure 7A). Adjacent cells had widely different numbers of fields (Figures 7B and 7C). There was a small correlation in the field numbers of nearby cells (all cell pairs with centers $<25\ \mu\text{m}$ apart; 4 mice: $r = 0.035\text{--}0.18$, $p < 0.001\text{--}0.50$). However, when we controlled for the moderate propensity gradient across superficial-deep (Mizuseki et al., 2011; Danielson et al., 2016) and proximal-distal axes (Henriksen et al., 2010) using a low-pass spatial filter, the correlation in field numbers of nearby cells disappeared (Figure 7D; see STAR Methods). Therefore, propensity is organized in a largely salt-and-pepper manner.

Unified Model of Hippocampal Representations

Bringing together the above results, we can describe at a statistical level how the hippocampus will represent spatial contexts under a wide range of conditions with a simple generative model we call the “(gamma \times gain) Poisson” model (Figure 7E). Each cell is randomly assigned a propensity drawn from the gamma distribution of propensities, due to its salt-and-pepper organization. Given its propensity, each cell randomly expresses place fields in a spatially Poisson manner (rate parameter = propensity). At rewarded places, every cell's propensity is multiplied

by a common gain factor (similarly in novel environments, by a different common factor). Finally, each cell's propensity predicts its activity independent of environmental context and is highly preserved for a month or more. The key parameter underlying all aspects of the model is the cell's propensity. Modifications to the model to account for additional details would include a shift of the gamma distribution to slightly lower (higher) mean propensities for more superficial (deep) and proximal (distal) regions of CA1, a small deviation of reward propensity from a constant gain times the non-reward propensity, and a small drift of propensity values over time.

Intracellular Mechanisms Underlying Differences in Propensity

The preservation of each cell's propensity (or relative propensity via multiplicative scaling) in a variety of conditions suggests a cell-intrinsic factor like excitability underlies propensity. We therefore investigated intracellular CA1 pyramidal cell recordings ($n = 21$) in mice exploring familiar, standard-size ($\sim 2\ \text{m}$) virtual environments (Cohen et al., 2017). Each cell's mean subthreshold membrane potential (V_m) exhibited multiple peaks as a function of the animal's location, reflecting spatially tuned inputs to the cell (Figure 7F). Peaks differed in amplitude across locations as well as across cells, and most were, as expected, below spike threshold (Figure S6A). Importantly, the mean amplitude of peaks significantly differed between cells (Figures 7G, S6B, and S6C, $p = 6e\text{--}42$), and cells with larger peaks had higher baseline V_m s and thresholds closer to baseline (Figures S6D and S6E), consistent with the idea that cells differ in excitability (Epsztein et al., 2011) and that higher excitability cells amplify their inputs more (Lee et al., 2012). The V_m was $1.34 \times$ larger in consistently rewarded areas (Figure 7H). We ran a probabilistic simulation based on the observed distribution of peak amplitudes within and across cells, including the relationship to threshold – (minus) baseline and effect of reward. This simulation, which incorporated the excitability differences seen in the data as a central element, produced the distribution of field numbers and reward activity seen in large environments (Figures 7I and S6F–S6H; constant gain copula correlation: 1.0).

We then explored what biophysical mechanisms could underlie excitability differences and result in the observed intracellular and imaging data. Persistent sodium current (I_{NaP}) amplifies inputs to CA1 neurons (Hsu et al., 2018). We simulated single-compartment Hodgkin-Huxley-type neuron models (Sherfey et al., 2018) in which all cells received the same Gaussian distribution of spatial inputs (as seen in the intracellular data; see STAR Methods) and the same additive boost to input in rewarded areas. The only difference between cells was the amount of I_{NaP} , with more I_{NaP} increasing excitability and thus propensity (Figure S7). We determined the I_{NaP} distribution across cells that best fit the intracellular data (Figure S7C), then used this distribution (whose mean ended up matching measured I_{NaP} values) (Durstewitz et al., 2000) to simulate activity in large environments. This produced a skewed field number distribution, correlated reward and non-reward activity, and also the observed correlation of peak V_m amplitude with baseline and anticorrelation with threshold – baseline (Figure S7E). The constant gain copula model provided a good fit to the distribution of reward and

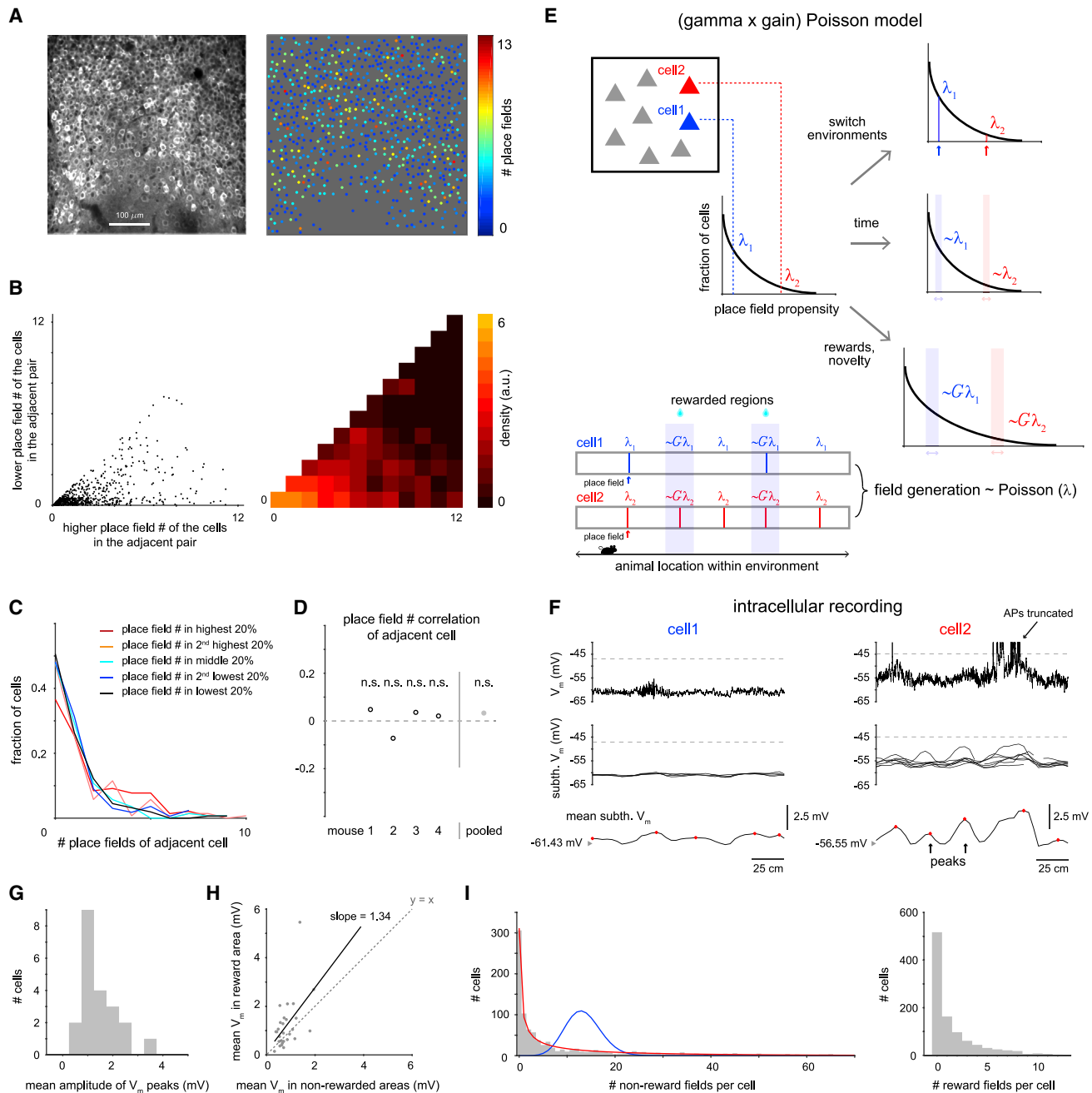


Figure 7. Widely Different Propensities between Cells Are Anatomically Arranged in a Salt-and-Pepper Fashion and Can Be Explained by Differences in Features of Intracellularly Recorded Cells

- (A) Standard deviation image of GCaMP6f signal and place field numbers of corresponding cells.
- (B) Plot (jittered, left) of field numbers of each pair of cells with centers <25 μm apart (mouse 1). Corresponding density (right). Adjacent cells have widely different field numbers.
- (C) Distribution of field number of cells <25 μm away from cells with field numbers in a given propensity quintile (mouse 1).
- (D) Correlation of field numbers for pairs of cells <25 μm apart, corrected for known propensity gradient across anatomical axes.
- (E) Schematic of “(gamma x gain) Poisson” model of hippocampal representations based on the findings in this study. Note the value of G is generally different for reward versus novelty.
- (F) Intracellular CA1 recordings of mice in (~2 m) virtual environments. Raw V_m trace of 1 lap as function of location (top) (note: except here, V_m refers to sub-threshold V_m in rest of this figure and Figures S6 and S7). Mean subthreshold V_m per lap (middle). Mean V_m across laps with peaks identified (bottom).
- (G) Distribution of mean of amplitudes of V_m peaks per cell ($n = 21$).

(legend continued on next page)

non-reward fields (correlation: 0.99). Therefore, differences in I_{NaP} (or, presumably, other voltage-dependent conductances) appear sufficient to explain the observed propensity distributions.

DISCUSSION

Here, we show that a single function, the field propensity distribution, underlies many fundamental features of hippocampal activity. A cell's propensity dictates how many place fields it will have, how likely it will respond at rewarded locations, applies to any environment, familiar or novel, and is a stable property of the cell over time. This—combined with our previous finding that a cell's fields are randomly located given its propensity (Rich et al., 2014) (Figure S2, legend)—implies propensity is the key parameter determining the structure of hippocampal representations. We also found propensity is distributed in a largely salt-and-pepper manner. All these features are captured by the compact “(gamma \times gain) Poisson” model (Figure 7E). Our results reveal persistent, order-of-magnitude differences between CA1 pyramidal cells in the feature these cells are most well-known for—having place fields. That is, the probability of representing any given location, context, or other item (e.g., a rewarded location) greatly and consistently varies across cells, with some cells being active in the representations of many items and others in only a very select subset of them. These large differences strongly shape the hippocampal representation of any given environmental context and thus very likely impact how the spatial code—and presumably the code for episodic memory in the human hippocampus (Gelbard-Sagiv et al., 2008)—is encoded, read out, or associated with other behaviorally relevant information. For instance, the sparse code among low propensity cells allows simple mechanisms for readout of, and forming associations with, specific locations (Olshausen and Field, 2004).

Previous work using smaller (~ 1 m) environments showed (1) average firing rates of hippocampal cells are skewed and correlated across sleep/wake states and across environments experienced within a day (Hirase et al., 2001; Mizuseki and Buzsáki, 2013), but (2) activity levels change substantially over hours to a week using a binary measure of propensity, i.e., whether each cell was a place or silent cell (Ziv et al., 2013; Rubin et al., 2015; Cai et al., 2016). Because firing rate and number of fields are likely correlated, (1) is consistent with preservation of propensity across environments experienced on the same day, while (2) indicates propensity changes over time. Here, tracking cells over months in multiple large environments enabled us to determine propensity is instead highly preserved across time and environments. We could explain the variable number of fields a cell had across environments and time as resulting from a fixed propensity's Poisson noise, plus some global modulation of the whole propensity distribution, and a small amount of drift over time. The difference from previous results could be due to our use of larger environments, as the larger range of field

numbers allow a higher resolution measure of propensity than binary assessment, or because of differences in the animal's experience and encoding.

Previous work showed elevated preservation of propensity between experiences occurring within hours (Cai et al., 2016) and attributed it to transient, activity-dependent increases of excitability in recently active cells (Han et al., 2007; Silva et al., 2009; Zhou et al., 2009; Cai et al., 2016; Rashid et al., 2016). Our data also showed higher preservation of propensity across environments explored on the same day. However, the dominant trend we found was preservation of propensity with minor degradation over a month (Figure 4E), including across months in a home cage without task experience (Figure 4C), suggesting a large contribution of non-activity-dependent mechanisms for preserving propensity. Note, although we observed global remapping, constant elements (head fixation, treadmill) could contribute to preserved propensity across environments. However, freely moving animals have similar within-day propensities (Cai et al., 2016) and firing rates (Mizuseki and Buzsáki, 2013), showing preservation across contexts independent of experimental details.

Previous work found moderate gradients in propensity along major anatomical axes (Henriksen et al., 2010; Mizuseki et al., 2011; Danielson et al., 2016), which we observed here too. However, we found that cells with $\sim 10\times$ differences in propensity were distributed in salt-and-pepper fashion, superimposed on the gradual $\sim 30\%-40\%$ changes in mean field number along proximal-distal and superficial-deep axes observed before.

Unlike previous work, we studied propensity and reward activity together and discovered they are tightly related. The increased field density around reward locations was well-explained by multiplication of each cell's propensity by a constant gain. Other work instead attributed reward-related increases to a small subset ($\sim 5\%$) of cells active only at rewarded, and not at non-rewarded, locations (Gauthier and Tank, 2018; Sato et al., 2018). Our data did have $\sim 5\%$ of cells with ≥ 1 reward field and 0 non-reward fields, but our model could account for them as cells that could have non-reward fields but did not by chance (Figure 6E) (although we cannot rule out a possibly very small set of reward-specific cells). In contrast to the other work, the excess field density at reward locations could not be explained by cells only activated by reward (Figures 5G and 5H). Thus, our results are consistent with all cells receiving reward input. This supports conjunctive reward \times place coding, which could guide navigation to a specific rewarded location over other rewarded locations. The differences could be due to our use of large environments with 4 reward locations each, instead of smaller ($\sim 2\text{--}4$ m) environments with 1 reward location. We could also explain higher activity in novel environments by multiplicative scaling of propensity (with different gain than reward), supporting the generality of the “(gamma \times gain) Poisson” model. We speculate propensities change multiplicatively in cue rich or poor regions without reward (Sato et al., 2018; Bourboulou

(H) Mean V_m in consistently rewarded versus non-rewarded areas in each cell. Linear regression (solid).

(I) Non-reward and reward field number per cell distributions from large environment simulation based on parameters from intracellular recordings (mean of 100 simulations). See STAR Methods.

See also Figures S6 and S7.

et al., 2019), the key being that relative propensities are preserved via scaling with a gain common to all cells in a given location or situation.

The preservation of each cell's propensity across conditions suggests a modified view of the origin of receptive fields such as place fields. Receptive field models generally focus on the number and strength of inputs as determining a cell's output, i.e., “output \sim input” with small excitability variations relative to variations in inputs. However, while our findings are consistent with inputs determining tuning (i.e., field locations), they suggest that whether tuned inputs lead to output (i.e., field number) strongly depends on a global, excitability-based property of each postsynaptic cell. That is, “output \sim input \times excitability,” with large variations in excitability controlling the level of output.

This picture is supported by intracellular place and silent cell recordings in behaving animals. These recordings showed that hippocampal neurons differ in intrinsic excitability and place field activity correlates with excitability (Epsztain et al., 2011; Cohen et al., 2017), and that manipulating excitability controls whether spatially tuned inputs are converted into place field spiking by amplifying them (Lee et al., 2012; Hsu et al., 2018). They also revealed inputs are spatially tuned across the entire environment, with multiple subthreshold V_m peaks versus location whether a cell is active or not (Cohen et al., 2017; Hsu et al., 2018) (Figure 7F). Such tuning provides each cell with many potential place fields from which any number can be converted to output depending on cell excitability (Lee et al., 2012). Excitability would underlie a cell's propensity by setting how much it amplifies responses to any inputs. In strong support of this, we found that the average amplitude of subthreshold peaks differs significantly between cells, this amplitude is correlated with other excitability-related intracellular features (Figures S6D and S6E), and excitability-based input amplification models quantitatively matched to the intracellular data produce the observed propensity distribution (Figures 7I, S6, and S7). The spatial Poisson randomness of field locations would arise from effectively thresholding the sum of the many spatially tuned inputs to the cell. Alternatively, differences in the number, strength, and/or distribution (Druckmann et al., 2014) of inputs to each cell could contribute to propensity differences (e.g., by triggering more plateau potentials and field formation) (Bittner et al., 2015, 2017). However, place and silent cells' bursting patterns to intracellular current injection differed when inputs were inactive (just after seal formation, when low-calcium internal solution remained around the cell) (Epsztain et al., 2011), supporting a cell-intrinsic basis of propensity. Multiple approaches also showed excitability can bias which cells will represent fear memories in amygdala (Han et al., 2007; Silva et al., 2009; Zhou et al., 2009; Rashid et al., 2016) and hippocampus (Cai et al., 2016). Input and excitability differences could also together underlie propensity differences.

What mechanisms underlie the order-of-magnitude range of propensities across neighboring neurons that have generally been considered a single cell type (dorsal CA1 pyramidal cells at the same superficial-deep and proximal-distal location)? Excitability and other cellular or local circuit property gradients along proximal-distal or superficial-deep axes (Jarsky et al., 2008; Graves et al., 2012; Lee et al., 2014b; Valero et al., 2015) could explain the ~30%–40% differences in propensity reported

along these axes (Henriksen et al., 2010; Mizuseki et al., 2011; Danielson et al., 2016) but not the larger propensity fluctuations between adjacent cells observed here. The persistence and apparent cell-intrinsic basis of propensity differences suggest transcriptomic differences, possibly arising in development (Ziesel et al., 2015; Cembrowski et al., 2016; Mallory and Giocomo, 2018; Soltesz and Losonczy, 2018). In line with this, we show a biophysical model fit to intracellular data, in which only I_{NaP} differs across cells, is sufficient to explain the distribution of propensities (Figure S7). Morphological differences may also contribute (Diamantaki et al., 2016). Reward-based propensity increases could arise from amplification by entorhinal cortex inputs (Jarsky et al., 2005; Dudman et al., 2007; Basu et al., 2016) of CA3 inputs, because CA3 shows no field density increase in rewarded places (Dupret et al., 2010).

The persistent distribution of propensities seen here allows the simultaneous existence of a sparse code, dense code, and everything in between among pre-specified subsets of neurons. The sparse code for location, including rewarded places, could be used for goal-directed navigation. A wide range of propensities may ensure enough cells participate in distinguishing environments of any size (Rich et al., 2014), e.g., high propensity cells would ensure the engram (Liu et al., 2012) consisting of all cells with fields in a small environment is not proportionately small. CA1 cells encoding novel environments tend to have fewer fields (Grosmark and Buzsáki, 2016), potentially linking propensity with plasticity.

The large, persistent propensity differences we observed among nominally similar cells could be a general organizing principle for other brain areas, especially those that learn distributed representations of arbitrary internal or external stimuli (Rigotti et al., 2013). A skewed propensity distribution is seen in the fly mushroom body, where many Kenyon cells respond to a few odors and a few to many odors (Turner et al., 2008). Rat visual cortex neurons exhibit a wide range of firing rates that persist >1 week (Hengen et al., 2016). Given a particular propensity distribution, memory capacity (in terms of the number of distinct representations) is maximized if each cell is randomly selective for stimuli (e.g., locations) at a rate constrained by its propensity, as shown for CA1 (Rich et al., 2014) (Figure S2). The persistently low propensity cells would yield a sparse code for whichever stimulus space is represented. The high propensity cells could ensure enough cells represent each stimulus and facilitate associating representations via overlap.

STAR★METHODS

Detailed methods are provided in the online version of this paper and include the following:

- KEY RESOURCES TABLE
- RESOURCE AVAILABILITY
 - Lead Contact
 - Materials Availability
 - Data and Code Availability
- EXPERIMENTAL MODEL AND SUBJECT DETAILS
- METHOD DETAILS
 - Chronic imaging window surgery

- Virtual reality and behavioral setup
- Behavioral training
- Immunohistochemistry for GABAergic neurons
- Two-photon calcium imaging
- Intracellular recording
- **QUANTIFICATION AND STATISTICAL ANALYSIS**
 - Data analysis (general)
 - Calcium imaging analysis
 - Detecting calcium activity
 - Determination of place fields
 - Determination of reward fields
 - Place field number correlation
 - Population vector correlation
 - Place field shift analysis
 - Bayesian decoding
 - Place field variance explained by a model where each cell has a fixed, cell-specific propensity
 - Place field number, across session model (*Figures 4D and 4E*)
 - Place field number, reward field number model (*Figure 6*)
 - Place field number, spatial correlation (*Figure 7D*)
 - Intracellular recording analysis
 - Probabilistic simulation of field propensity distribution based on intracellular data
 - Biophysical model of field propensity distribution centered on INaP differences and fit to intracellular data

ACKNOWLEDGMENTS

We thank N. Sofroniew, K. Svoboda, V. Goncharov, I. Negashov, S. Taylor, J. Arnold, J. Osborne, B. Biddle, B. Bowers, and M. Bolstad for technical assistance. This work was supported by the Howard Hughes Medical Institute.

AUTHOR CONTRIBUTIONS

J.S.L. and A.K.L. designed the experiments; J.S.L. performed the imaging experiments; J.D.C. performed the intracellular experiments; J.S.L. and J.J.B. performed the imaging analysis with input from A.K.L. and S.R.; J.S.L. and J.D.C. performed the intracellular analysis with input from A.K.L., S.R., and J.J.B.; J.J.B. and S.R. constructed the statistical models with input from A.K.L.; J.S.L. constructed the intracellular models with input from A.K.L., S.R., J.D.C., and J.J.B.; and A.K.L., J.S.L., J.J.B., and S.R. wrote the paper.

DECLARATION OF INTERESTS

The authors declare no competing interests.

Received: April 23, 2019

Revised: May 25, 2020

Accepted: September 9, 2020

Published: October 8, 2020

REFERENCES

- Alme, C.B., Miao, C., Jezek, K., Treves, A., Moser, E.I., and Moser, M.B. (2014). Place cells in the hippocampus: eleven maps for eleven rooms. *Proc. Natl. Acad. Sci. USA* **111**, 18428–18435.
- Basu, J., Zaremba, J.D., Cheung, S.K., Hitti, F.L., Zemelman, B.V., Losonczy, A., and Siegelbaum, S.A. (2016). Gating of hippocampal activity, plasticity, and memory by entorhinal cortex long-range inhibition. *Science* **351**, aaa5694.
- Bittner, K.C., Grienberger, C., Vaidya, S.P., Milstein, A.D., Macklin, J.J., Suh, J., Tonegawa, S., and Magee, J.C. (2015). Conjunctive input processing drives feature selectivity in hippocampal CA1 neurons. *Nat. Neurosci.* **18**, 1133–1142.
- Bittner, K.C., Milstein, A.D., Grienberger, C., Romani, S., and Magee, J.C. (2017). Behavioral time scale synaptic plasticity underlies CA1 place fields. *Science* **357**, 1033–1036.
- Bourboulou, R., Marti, G., Michon, F.X., El Fegaly, E., Nouguier, M., Robbe, D., Koenig, J., and Epsztain, J. (2019). Dynamic control of hippocampal spatial coding resolution by local visual cues. *eLife* **8**, e44487.
- Buzsáki, G., and Mizuseki, K. (2014). The log-dynamic brain: how skewed distributions affect network operations. *Nat. Rev. Neurosci.* **15**, 264–278.
- Cai, D.J., Aharoni, D., Shuman, T., Shobe, J., Biane, J., Song, W., Wei, B., Veshkini, M., La-Vu, M., Lou, J., et al. (2016). A shared neural ensemble links distinct contextual memories encoded close in time. *Nature* **534**, 115–118.
- Gembrowski, M.S., Bachman, J.L., Wang, L., Sugino, K., Shields, B.C., and Spruston, N. (2016). Spatial gene-expression gradients underlie prominent heterogeneity of CA1 pyramidal neurons. *Neuron* **89**, 351–368.
- Cohen, J.D., Bolstad, M., and Lee, A.K. (2017). Experience-dependent shaping of hippocampal CA1 intracellular activity in novel and familiar environments. *eLife* **6**, e23040.
- Dana, H., Chen, T.W., Hu, A., Shields, B.C., Guo, C., Looger, L.L., Kim, D.S., and Svoboda, K. (2014). Thy1-GCaMP6 transgenic mice for neuronal population imaging in vivo. *PLoS ONE* **9**, e108697.
- Danielson, N.B., Zaremba, J.D., Kaifosh, P., Bowler, J., Ladow, M., and Losonczy, A. (2016). Sublayer-specific coding dynamics during spatial navigation and learning in hippocampal area CA1. *Neuron* **91**, 652–665.
- Davidson, T.J., Kloosterman, F., and Wilson, M.A. (2009). Hippocampal replay of extended experience. *Neuron* **63**, 497–507.
- Deshmukh, S.S., and Knierim, J.J. (2013). Influence of local objects on hippocampal representations: Landmark vectors and memory. *Hippocampus* **23**, 253–267.
- Diamantaki, M., Frey, M., Berens, P., Preston-Ferrer, P., and Burgalossi, A. (2016). Sparse activity of identified dentate granule cells during spatial exploration. *eLife* **5**, e20252.
- Dombeck, D.A., Harvey, C.D., Tian, L., Looger, L.L., and Tank, D.W. (2010). Functional imaging of hippocampal place cells at cellular resolution during virtual navigation. *Nat. Neurosci.* **13**, 1433–1440.
- Druckmann, S., Feng, L., Lee, B., Yook, C., Zhao, T., Magee, J.C., and Kim, J. (2014). Structured synaptic connectivity between hippocampal regions. *Neuron* **81**, 629–640.
- Dubbs, A., Guevara, J., and Yuste, R. (2016). moco: Fast motion correction for calcium imaging. *Front. Neuroinform.* **10**, 6. <https://doi.org/10.3389/fninf.2016.00006>.
- Dudman, J.T., Tsay, D., and Siegelbaum, S.A. (2007). A role for synaptic inputs at distal dendrites: instructive signals for hippocampal long-term plasticity. *Neuron* **56**, 866–879.
- Dupret, D., O'Neill, J., Pleydell-Bouverie, B., and Csicsvari, J. (2010). The reorganization and reactivation of hippocampal maps predict spatial memory performance. *Nat. Neurosci.* **13**, 995–1002.
- Durstewitz, D., Seamans, J.K., and Sejnowski, T.J. (2000). Dopamine-mediated stabilization of delay-period activity in a network model of prefrontal cortex. *J. Neurophysiol.* **83**, 1733–1750.
- Epsztain, J., Brecht, M., and Lee, A.K. (2011). Intracellular determinants of hippocampal CA1 place and silent cell activity in a novel environment. *Neuron* **70**, 109–120.
- Fenton, A.A., Kao, H.Y., Neymotin, S.A., Olyfer, A., Vayntrub, Y., Lytton, W.W., and Ludvig, N. (2008). Unmasking the CA1 ensemble place code by exposures to small and large environments: more place cells and multiple, irregularly arranged, and expanded place fields in the larger space. *J. Neurosci.* **28**, 11250–11262.
- Gauthier, J.L., and Tank, D.W. (2018). A Dedicated Population for Reward Coding in the Hippocampus. *Neuron* **99**, 179–193.

- Geiller, T., Fattah, M., Choi, J.S., and Royer, S. (2017). Place cells are more strongly tied to landmarks in deep than in superficial CA1. *Nat. Commun.* 8, 14531.
- Gelbard-Sagiv, H., Mukamel, R., Harel, M., Malach, R., and Fried, I. (2008). Internally generated reactivation of single neurons in human hippocampus during free recall. *Science* 322, 96–101.
- Golomb, D., Yue, C., and Yaari, Y. (2006). Contribution of persistent Na⁺ current and M-type K⁺ current to somatic bursting in CA1 pyramidal cells: combined experimental and modeling study. *J. Neurophysiol.* 96, 1912–1926.
- Graves, A.R., Moore, S.J., Bloss, E.B., Mensh, B.D., Kath, W.L., and Spruston, N. (2012). Hippocampal pyramidal neurons comprise two distinct cell types that are countermodulated by metabotropic receptors. *Neuron* 76, 776–789.
- Grosmark, A.D., and Buzsáki, G. (2016). Diversity in neural firing dynamics supports both rigid and learned hippocampal sequences. *Science* 351, 1440–1443.
- Hainmueller, T., and Bartos, M. (2018). Parallel emergence of stable and dynamic memory engrams in the hippocampus. *Nature* 558, 292–296.
- Han, J.H., Kushner, S.A., Yiu, A.P., Cole, C.J., Matynia, A., Brown, R.A., Neve, R.L., Guzowski, J.F., Silva, A.J., and Josselyn, S.A. (2007). Neuronal competition and selection during memory formation. *Science* 316, 457–460.
- Harvey, C.D., Collman, F., Dombeck, D.A., and Tank, D.W. (2009). Intracellular dynamics of hippocampal place cells during virtual navigation. *Nature* 461, 941–946.
- Hengen, K.B., Torrado Pacheco, A., McGregor, J.N., Van Hooser, S.D., and Turrigiano, G.G. (2016). Neuronal firing rate homeostasis is inhibited by sleep and promoted by wake. *Cell* 165, 180–191.
- Henriksen, E.J., Colgin, L.L., Barnes, C.A., Witter, M.P., Moser, M.B., and Moser, E.I. (2010). Spatial representation along the proximodistal axis of CA1. *Neuron* 68, 127–137.
- Hirase, H., Leinekugel, X., Czurkó, A., Csicsvari, J., and Buzsáki, G. (2001). Firing rates of hippocampal neurons are preserved during subsequent sleep episodes and modified by novel awake experience. *Proc. Natl. Acad. Sci. USA* 98, 9386–9390.
- Hodgkin, A.L., and Huxley, A.F. (1952). A quantitative description of membrane current and its application to conduction and excitation in nerve. *J. Physiol.* 117, 500–544.
- Hollup, S.A., Molden, S., Donnett, J.G., Moser, M.B., and Moser, E.I. (2001). Accumulation of hippocampal place fields at the goal location in an annular watermaze task. *J. Neurosci.* 21, 1635–1644.
- Hsu, C.L., Zhao, X., Milstein, A.D., and Spruston, N. (2018). Persistent sodium current mediates the steep voltage dependence of spatial coding in hippocampal pyramidal neurons. *Neuron* 99, 147–162.e8.
- Hubel, D.H., and Wiesel, T.N. (1962). Receptive fields, binocular interaction and functional architecture in the cat's visual cortex. *J. Physiol.* 160, 106–154.
- Jarsky, T., Roxin, A., Kath, W.L., and Spruston, N. (2005). Conditional dendritic spike propagation following distal synaptic activation of hippocampal CA1 pyramidal neurons. *Nat. Neurosci.* 8, 1667–1676.
- Jarsky, T., Mady, R., Kennedy, B., and Spruston, N. (2008). Distribution of bursting neurons in the CA1 region and the subiculum of the rat hippocampus. *J. Comp. Neurol.* 506, 535–547.
- Karlsson, M.P., and Frank, L.M. (2008). Network dynamics underlying the formation of sparse, informative representations in the hippocampus. *J. Neurosci.* 28, 14271–14281.
- Katkov, M., Romani, S., and Tsodyks, M. (2017). Memory retrieval from first principles. *Neuron* 94, 1027–1032.
- Kjelstrup, K.B., Solstad, T., Brun, V.H., Hafting, T., Leutgeb, S., Witter, M.P., Moser, E.I., and Moser, M.B. (2008). Finite scale of spatial representation in the hippocampus. *Science* 321, 140–143.
- Lee, A.K., Epsztein, J., and Brecht, M. (2009). Head-anchored whole-cell recordings in freely moving rats. *Nat. Protoc.* 4, 385–392.
- Lee, D., Lin, B.J., and Lee, A.K. (2012). Hippocampal place fields emerge upon single-cell manipulation of excitability during behavior. *Science* 337, 849–853.
- Lee, D., Shtengel, G., Osborne, J.E., and Lee, A.K. (2014a). Anesthetized- and awake-patched whole-cell recordings in freely moving rats using UV-cured collar-based electrode stabilization. *Nat. Protoc.* 9, 2784–2795.
- Lee, S.H., Marchionni, I., Bezaire, M., Varga, C., Danielson, N., Lovett-Barron, M., Losonczy, A., and Soltesz, I. (2014b). Parvalbumin-positive basket cells differentiate among hippocampal pyramidal cells. *Neuron* 82, 1129–1144.
- Leutgeb, S., Leutgeb, J.K., Barnes, C.A., Moser, E.I., McNaughton, B.L., and Moser, M.B. (2005). Independent codes for spatial and episodic memory in hippocampal neuronal ensembles. *Science* 309, 619–623.
- Liu, X., Ramirez, S., Pang, P.T., Puryear, C.B., Govindarajan, A., Deisseroth, K., and Tonegawa, S. (2012). Optogenetic stimulation of a hippocampal engram activates fear memory recall. *Nature* 484, 381–385.
- Lovett-Barron, M., Kaifosh, P., Kheirbek, M.A., Danielson, N., Zaremba, J.D., Reardon, T.R., Turi, G.F., Hen, R., Zemelman, B.V., and Losonczy, A. (2014). Dendritic inhibition in the hippocampus supports fear learning. *Science* 343, 857–863.
- Mallory, C.S., and Giocomo, L.M. (2018). Heterogeneity in hippocampal place coding. *Curr. Opin. Neurobiol.* 49, 158–167.
- Malvache, A., Reichinnek, S., Villette, V., Haimerl, C., and Cossart, R. (2016). Awake hippocampal reactivations project onto orthogonal neuronal assemblies. *Science* 353, 1280–1283.
- Mankin, E.A., Sparks, F.T., Slayyeh, B., Sutherland, R.J., Leutgeb, S., and Leutgeb, J.K. (2012). Neuronal code for extended time in the hippocampus. *Proc. Natl. Acad. Sci. USA* 109, 19462–19467.
- Mankin, E.A., Diehl, G.W., Sparks, F.T., Leutgeb, S., and Leutgeb, J.K. (2015). Hippocampal CA2 activity patterns change over time to a larger extent than between spatial contexts. *Neuron* 85, 190–201.
- Mizuseki, K., and Buzsáki, G. (2013). Preconfigured, skewed distribution of firing rates in the hippocampus and entorhinal cortex. *Cell Rep.* 4, 1010–1021.
- Mizuseki, K., Diba, K., Pastalkova, E., and Buzsáki, G. (2011). Hippocampal CA1 pyramidal cells form functionally distinct sublayers. *Nat. Neurosci.* 14, 1174–1181.
- Morris, R.G., Garrud, P., Rawlins, J.N., and O'Keefe, J. (1982). Place navigation impaired in rats with hippocampal lesions. *Nature* 297, 681–683.
- Mountcastle, V.B. (1957). Modality and topographic properties of single neurons of cat's somatic sensory cortex. *J. Neurophysiol.* 20, 408–434.
- Muller, R.U., and Kubie, J.L. (1987). The effects of changes in the environment on the spatial firing of hippocampal complex-spike cells. *J. Neurosci.* 7, 1951–1968.
- Nelsen, R.B. (1999). *An Introduction to Copulas* (Springer).
- Nitz, D., and McNaughton, B. (2004). Differential modulation of CA1 and dentate gyrus interneurons during exploration of novel environments. *J. Neurophysiol.* 91, 863–872.
- O'Keefe, J. (1976). Place units in the hippocampus of the freely moving rat. *Exp. Neurol.* 51, 78–109.
- O'Keefe, J., and Conway, D.H. (1978). Hippocampal place units in the freely moving rat: why they fire where they fire. *Exp. Brain Res.* 31, 573–590.
- O'Keefe, J., and Dostrovsky, J. (1971). The hippocampus as a spatial map. Preliminary evidence from unit activity in the freely-moving rat. *Brain Res.* 34, 171–175.
- Olshausen, B.A., and Field, D.J. (2004). Sparse coding of sensory inputs. *Curr. Opin. Neurobiol.* 14, 481–487.
- Penfield, W., and Boldrey, E. (1937). Somatic motor and sensory representation in the cerebral cortex of man as studied by electrical stimulation. *Brain* 60, 389–443.
- Rashid, A.J., Yan, C., Mercaldo, V., Hsiang, H.L.L., Park, S., Cole, C.J., De Cristofaro, A., Yu, J., Ramakrishnan, C., Lee, S.Y., et al. (2016). Competition between engrams influences fear memory formation and recall. *Science* 353, 383–387.
- Rich, P.D., Liaw, H.P., and Lee, A.K. (2014). Place cells. Large environments reveal the statistical structure governing hippocampal representations. *Science* 345, 814–817.

- Rigotti, M., Barak, O., Warden, M.R., Wang, X.J., Daw, N.D., Miller, E.K., and Fusi, S. (2013). The importance of mixed selectivity in complex cognitive tasks. *Nature* 497, 585–590.
- Rubin, A., Geva, N., Sheintuch, L., and Ziv, Y. (2015). Hippocampal ensemble dynamics timestamp events in long-term memory. *eLife* 4, e12247.
- Sato, M., Mizuta, K., Islam, T., Kawano, M., Takekawa, T., Gomez-Dominguez, D., Kim, K., Yamakawa, H., Ohkura, M., and Fukai, T. (2018). Dynamic embedding of salience coding in hippocampal spatial maps. *bioRxiv*. <https://doi.org/10.1101/266767>.
- Seelig, J.D., Chiappe, M.E., Lott, G.K., Dutta, A., Osborne, J.E., Reiser, M.B., and Jayaraman, V. (2010). Two-photon calcium imaging from head-fixed *Drosophila* during optomotor walking behavior. *Nat. Methods* 7, 535–540.
- Sheffield, M.E., and Dombeck, D.A. (2015). Calcium transient prevalence across the dendritic arbor predicts place field properties. *Nature* 517, 200–204.
- Sherfey, J.S., Soplapata, A.E., Ardid, S., Roberts, E.A., Stanley, D.A., Pittman-Polletta, B.R., and Kopell, N.J. (2018). DynaSim: A MATLAB toolbox for neural modeling and simulation. *Front. Neuroinform.* 12, 10.
- Silva, A.J., Zhou, Y., Rogerson, T., Shobe, J., and Balaji, J. (2009). Molecular and cellular approaches to memory allocation in neural circuits. *Science* 326, 391–395.
- Soltesz, I., and Losonczy, A. (2018). CA1 pyramidal cell diversity enabling parallel information processing in the hippocampus. *Nat. Neurosci.* 21, 484–493.
- Talbot, S., and Marshall, W. (1941). Physiological studies on neural mechanisms of visual localization and discrimination. *Am. J. Ophthalmol.* 24, 1255–1264.
- Thompson, L.T., and Best, P.J. (1989). Place cells and silent cells in the hippocampus of freely-behaving rats. *J. Neurosci.* 9, 2382–2390.
- Tsodyks, M., and Feigelman, M. (1988). Enhanced storage capacity in neural networks with low level of activity. *Europhys. Lett.* 6, 101–105.
- Turner, G.C., Bazhenov, M., and Laurent, G. (2008). Olfactory representations by *Drosophila* mushroom body neurons. *J. Neurophysiol.* 99, 734–746.
- Valero, M., Cid, E., Averkin, R.G., Aguilar, J., Sanchez-Aguilera, A., Viney, T.J., Gomez-Dominguez, D., Bellistri, E., and de la Prida, L.M. (2015). Determinants of different deep and superficial CA1 pyramidal cell dynamics during sharp-wave ripples. *Nat. Neurosci.* 18, 1281–1290.
- Wilson, M.A., and McNaughton, B.L. (1993). Dynamics of the hippocampal ensemble code for space. *Science* 261, 1055–1058.
- Witharana, W.K.L., Cardiff, J., Chawla, M.K., Xie, J.Y., Alme, C.B., Eckert, M., Lapointe, V., Demchuk, A., Maurer, A.P., Trivedi, V., et al. (2016). Nonuniform allocation of hippocampal neurons to place fields across all hippocampal sub-fields. *Hippocampus* 26, 1328–1344.
- Zaremba, J.D., Diamantopoulou, A., Danielson, N.B., Grosmark, A.D., Kaifosh, P.W., Bowler, J.C., Liao, Z., Sparks, F.T., Gogos, J.A., and Losonczy, A. (2017). Impaired hippocampal place cell dynamics in a mouse model of the 22q11.2 deletion. *Nat. Neurosci.* 20, 1612–1623.
- Zeisel, A., Muñoz-Manchado, A.B., Codeluppi, S., Lönnberg, P., La Manno, G., Juréus, A., Marques, S., Munguba, H., He, L., Betsholtz, C., et al. (2015). Brain structure. Cell types in the mouse cortex and hippocampus revealed by single-cell RNA-seq. *Science* 347, 1138–1142.
- Zhou, Y., Won, J., Karlsson, M.G., Zhou, M., Rogerson, T., Balaji, J., Neve, R., Poirazi, P., and Silva, A.J. (2009). CREB regulates excitability and the allocation of memory to subsets of neurons in the amygdala. *Nat. Neurosci.* 12, 1438–1443.
- Ziv, Y., Burns, L.D., Cocker, E.D., Hamel, E.O., Ghosh, K.K., Kitch, L.J., El Gamal, A., and Schnitzer, M.J. (2013). Long-term dynamics of CA1 hippocampal place codes. *Nat. Neurosci.* 16, 264–266.

STAR★METHODS

KEY RESOURCES TABLE

REAGENT or RESOURCE	SOURCE	IDENTIFIER
Antibodies		
Anti-GAD67, clone 1G10.2 (monoclonal antibody, mouse)	Millipore	Cat# MAB5406; RRID: AB_2278725
Goat anti-mouse IgG2a cross-adsorbed secondary antibody, Alexa Fluor 647 conjugated	Thermo Fisher Scientific	Cat# A-21241; RRID: AB_2535810
Experimental Models: Organisms/Strains		
Mouse: C57BL/6J-Tg(Thy1-GCaMP6f)GP5.17Dkim/J	Janelia GENIE Project	JAX: 025393
Mouse: C57BL/6	Charles River Laboratories	C57BL/6NCrl
Software and Algorithms		
MouseoVeR / Jovian (for virtual reality)	Cohen et al., 2017	https://github.com/JaneliaSciComp/CohenBolstadLee_eLife2017
MOCO (motion correction for imaging)	Dubbs et al., 2016	https://github.com/NTCColumbia/moco
ROI selection	This paper	https://github.com/LeeA-Lab/2P_calculium_imaging

RESOURCE AVAILABILITY

Lead Contact

Further information and requests for resources should be directed to and will be fulfilled by the Lead Contact, Albert Lee (leea@janelia.hhmi.org).

Materials Availability

This study did not generate new unique reagents.

Data and Code Availability

The experimental and processing code used in this study are available at https://github.com/LeeA-Lab/2P_calculium_imaging (generated for this study), https://github.com/JaneliaSciComp/CohenBolstadLee_eLife2017 (Cohen et al., 2017), and <https://github.com/NTCColumbia/moco> (Dubbs et al., 2016). All data and other code are available from the Lead Contact upon request.

EXPERIMENTAL MODEL AND SUBJECT DETAILS

All procedures were performed in accordance with the Janelia Research Campus Institutional Animal Care and Use Committee guidelines on animal welfare. For imaging experiments, male GCaMP6f (Thy1-GCaMP6f-WPRE) transgenic mice (Dana et al., 2014) were used, 8–10 weeks old at the time of surgery. For intracellular recording experiments, 8–12 week-old male wild-type C57BL/6 mice (Charles River Laboratories) were used.

METHOD DETAILS

Chronic imaging window surgery

Four male GCaMP6f mice were used for all the imaging experiments in this study. Mice were anesthetized with isoflurane (1.5%–2.0%) and a craniotomy was centered at –2.0 mm AP and 1.6 mm ML from bregma over the left hemisphere using a 3 mm diameter trephine drill bit (Trepbine Bur, 3.0/2.0mm, THB30, Osung USA). The cortex and corpus callosum, but not alveus, above the dorsal hippocampus was removed by gentle suction with saline using a 27 gauge blunt-tip needle. After cortex / callosum removal, a glass coverslip (T 0.1 mm, D 3 mm, round, No.0, Warner Instruments, CS-3R-0) that was previously attached (using (Norland Optical adhesive 81) to the bottom of stainless steel cannula (OD 3.02 mm, ID 2.54 mm, L 1.75 mm, New England Small Tube Corp. Type 304, stainless steel, 11TW) was implanted over the dorsal CA1 region. A thin layer of Kwik-Sil (WPI) was applied between the cannula and skull. The top part of the cannula and custom headplate (stainless or titanium) were fixed to the skull using dental cement (Meta-bond) and dental acrylic. Body temperature was maintained at 37°C using a temperature controlled heating pad.

Virtual reality and behavioral setup

We used our custom-made virtual reality (VR) software ‘MouseoVeR’ and spherical treadmill system which were described in detail previously (Cohen et al., 2017). Briefly, MouseoVeR (https://github.com/JaneliaSciComp/CohenBolstadLee_eLife2017) is part of Janelia’s open-source virtual reality software platform, Jovian. Our 40 cm-diameter spherical treadmill floats on multiple, air-supported ping pong balls (<https://www.janelia.org/open-science/large-spherical-treadmill-rodents>), and the treadmill’s movements are tracked by a modified version of FlyFizz (<https://wiki.janelia.org/wiki/display/flyfizz/Home>) (Seelig et al., 2010). Here, instead of using three projectors that projected onto the back of a screen with 225° field of view, for the imaging experiments we used a single projector that projected off a flat then convex mirror onto the front surface of a 180° cylindrical screen. The vertical field of view was from 20° below to 60° above the horizontal plane through the animal. A horizontal 145°-wide rendered view image in MouseoVeR was projected onto the 180° screen and the image distortion from the convex mirror was compensated using a function in MouseoVeR. We used the blue channel of the projector only and, in addition, a blue filter was located in front of projector (Valley design, FG-B03_3). Water drops were delivered via a metal tube that was fixed in place in front of the animal and straddled by a photobeam to detect licks.

Behavioral training

For the imaging experiments, four large virtual environments were made in Blender software. Each environment had a narrow ~14-cm-wide ~41-m-long winding path of different shapes that the mice were constrained to follow. Features of various spatial scales were placed around the environment, with smaller objects placed along the track to provide optic flow when running. The animal’s virtual view was constrained to be parallel to the track but they were allowed to move side-to-side within the width of the path. To help mice discriminate between the different environmental contexts, we also had a different, constant background odor cue (banana, cinnamon, lemon or apple) present for each environment. A unique combination of environment and odor cue was used for each mouse, but for a given mouse the combination was consistent throughout training. The mice underwent initial VR training using four different smaller environments (oval, circular, linear, linear with 15° turns, total track length ~185–325 cm) for habituation to head fixation and running on the treadmill through virtual environments. After 3 days of this smaller environment training, mice were trained in the large environments and on each day ran a total of 8–12 runs in 1–3 environments (i.e., 4–8 consecutive runs per environment; a set of consecutive runs in a given environment = a session), with imaging performed on a subset of days (Figures S1A and S4A). On days when animals explored > 1 environment, there was a ~30 min gap between the sessions in each environment. At the end of each run, the animal was teleported back to the beginning of the environment’s track, the virtual view was locked at the start location for 5 s, then the animal was allowed to continue with the next run. To make mice run consistently, mice were placed on water-restriction (1.2–1.4 ml/day) at least 3 days before starting initial VR training. For the random reward condition, 2 µL drops of water were delivered at 40 random locations in each run (200 possible reward locations were evenly spaced along the entire path of an environment, and on each run reward was given at a random 2 out of every group of 10 adjacent locations, i.e., 1–10, 11–20, ..., 191–200). For the fixed reward condition, we used the same environments except there were 4 fixed reward locations (and in each reward location five 4 µL drops of water were delivered within a 25 cm segment of track). Supplemental water was given each day after VR behavior based on the amount of water delivered during behavior.

Immunohistochemistry for GABAergic neurons

GABAergic interneurons were stained in two GCaMP6f mice. Mice were perfused transcardially using 4% paraformaldehyde in phosphate buffered saline (PBS). Brains were kept in PBS containing 4% PFA for 24 h at 4 C. and washed with PBS before slicing. 40 µm thick coronal sections were made with a vibratome (Leica, VT1200S) and immersed in PBS. Brain slices were immersed in PBS containing 0.5% Triton X-100 (vol/vol) for 20 min at room temperature and then were transferred to a blocking solution (5% donkey serum (vol/vol), 0.1% Triton X-100 in PBS) for 2 h. Subsequently slices were incubated with primary antibodies in blocking solution for 24 h at 4 C. The primary antibodies were mouse monoclonal anti-GAD67 diluted 1:1000 (MAB5406; Millipore). After incubation, slices were washed three times for 10 min with PBS containing 0.1% Triton X-100 and were incubated with secondary antibodies in the blocking solution for 1 h. The secondary antibodies were Alexa Fluor 647-conjugated anti-mouse IgG2a antibody diluted 1:400 (A-21241; ThermoFisher Scientific). Slices were rinsed three times for 10 min with the PBS containing 0.1% Triton X-100 then were mounted on microscope slides. The fluorescence signal was visualized by the confocal microscopy (Nikon Eclipse Ti) using a CFI Plan Fluor 40X Oil NA 1.3 WD 0.2 objective.

Two-photon calcium imaging

Calcium imaging was performed with a custom-built two-photon microscope with a resonant scanner (Janelia Research Campus, MIMMS). The light source was a Chameleon Vision II (Coherent) laser tuned to 940 nm. The objective was a 16x water immersion lens (Nikon, 0.8 NA). Functional images were acquired using ScanImage (Vidrio) software. Imaging was done in one plane, the size of the imaging plane was 500 µm x 500 µm (512 × 512 pixels), and the sampling rate was 30 Hz. The same imaging plane was found on successive days by visual comparison with a saved image from the first day. We sealed the gap between the objective and implant using Blu Tack (Bostik) to prevent any VR projection light from interfering with the GCaMP6f fluorescence signal channel.

Intracellular recording

Whole-cell recordings were obtained from hippocampal CA1 pyramidal neurons in a previous study (Cohen et al., 2017). Briefly, 8–12 wk-old head-fixed male C57BL/6 mice explored virtual linear environments created and displayed by the same MouseoVeR VR software as in the imaging experiments, with differences being that the field of view was 225° instead of 180°, the environments were black, white, blue, and green instead of bluescale, and the environments were ~185–325 cm in total path length instead of ~41 m. Mice were water-restricted and artificially sweetened (acesulfame potassium, 4 mM) water reward (~2 µL per drop) was delivered as follows. Each environment had 1 or 2 consistently rewarded locations where 1–2 drops were provided on every lap when the animal traversed that location and, in addition, ~1–2 drops were delivered at a random location in each lap (considered as non-rewarded areas). Blind *in vivo* whole-cell current-clamp recordings of the V_m (sampled at 25 kHz, amplifier lowpass filter set to 5 kHz) were obtained from the right and left dorsal hippocampus in awake mice (Lee et al., 2009, 2014a). Mice explored both novel and familiar environments, and only data from familiar environments was analyzed here (since the main imaging analysis was done for familiar environments).

QUANTIFICATION AND STATISTICAL ANALYSIS

Data analysis (general)

Data analysis was performed using MATLAB, unless otherwise noted. Correlation was always the Pearson correlation. Statistical significance was set at 0.05 and was determined using the unpaired t test, or t-statistic (for testing if a correlation value was different than 0), unless otherwise noted. Values are reported as mean ± s.e.m., unless otherwise noted.

Calcium imaging analysis

Motion correction was done by MOCO (ImageJ plugin, <https://github.com/NTCColumbia/moco>) (Dubbs et. al. 2016). The reference image for motion correction was selected from the first run and was used for the rest of the day's data. Regions of interest (ROIs) were defined in each imaging day in MATLAB using custom-written software (https://github.com/LeeA-Lab/2P_calculim_imaging). Individual neurons were manually selected from a standard deviation image of the first run (100–160 s of imaging data). ROIs (selected pixel ± 4 or ± 3 pixels) were determined automatically within a 9×9 or 7×7 pixel region (chosen to match the size of cell somata and to avoid signal contamination from nearby cells) of the manually selected cell. An 81×81 or 49×49 correlation matrix of the first run fluorescence signals of the pixels with respect to each other was created (excluding the diagonal). Pixels with low correlation (below 0.45) or high correlation (over 0.85, to avoid non-active regions e.g., cell nucleus) of activity with all other pixels were excluded (note the results in Figure 4A were similar when using correlation cutoffs of 0.35–0.95 or 0.55–0.75: $p < 2.5e-14$ for all comparisons with these cutoffs). If less than 5 pairs of pixels remained (in case of cells with few or no calcium transients, i.e., silent cells) then we used the 20 brightest pixels. Fluorescence signals of pixels in each ROI were averaged and used for further analysis. $\Delta F/F_0$ was calculated as $(F - F_0) / F_0$, where F is the time series of raw fluorescence averaged over the pixels in an ROI, F_0 is the mode of a kernel density estimate (MATLAB function “ksdensity”) of F within a run (calculation was done for each run). ROIs from multiple days were aligned manually using custom-written software in MATLAB by matching across the superimposed standard deviation images from pairs of days.

Detecting calcium activity

Prior to detecting calcium transient events, we applied a Savitzky-Golay filter with 500 ms window (“sgolayfilt” function in MATLAB) on the $\Delta F/F_0$ trace of individual cells. We set the threshold for detecting a calcium event for each neuron at each point in time as the median plus three times the interquartile range of the fluorescence activity of a ± 8 s sliding frame (Malvache et. al. 2016). The calcium transient event was defined as the trace from the time of the threshold crossing until the trace fell below the threshold.

Determination of place fields

First, we rejected activity during periods when the forward running speed of the mice did not exceed 2 cm/s to exclude activity when the animal stopped or was grooming. The extent of each calcium transient was converted from time to location, with a bin size of 1 cm. Since there were always at least 4 runs, and sometimes just 4 runs, in a given environment in a given session, we only used the first 4 runs from each environment (session) for analysis. A place field was defined as a region that had calcium transient events in ≥ 2 runs whose extents came within 30 cm of each other in these first 4 runs. The place field region (size) started at the spatial bin of the beginning of the “leftmost” calcium transient and ended at the end of the “rightmost” calcium transient, including any gaps of up to 30 cm in between transients. (Note the results in Figure 4A were similar when using place field criteria of 15, 30, 45, or 60 cm extents and ≥ 2 or ≥ 3 runs: $p < 2e-4$ for all comparisons with these criteria.) To fit the distribution of the number of place fields per cell, we fit the MATLAB Poisson probability density function (for equal Poisson propensity model) and Negative binomial probability density function (for gamma-Poisson propensity model). The first and last 30 cm of the track were excluded since the animal was locked in (virtual) place at the beginning of each track at the start of each run for 5 s, and there was an identical end-of-track cue in all environments. In the case of the novel-familiar copula model analysis (Figures 6F and 6G), in order to account for the less stable fields in novel environments, 90 cm was used for the place field extent criterion for both the novel and familiar sessions.

Determination of reward fields

A place field occurring in a fixed reward area (i.e., the field width overlapped the reward area) was called a reward field. Each reward area included the 25-cm-long reward delivery area, and 25 cm before and 75 cm after the delivery area, i.e., a 125-cm-long segment, which was empirically determined to be the region in which the place field density was increased (Figure 5C). (Note the results in Figure 5F were similar when using reward area definitions of 15 cm before and 50 cm after or 35 cm before and 100 cm after the delivery area, and place field criteria of 15, 30, or 45 cm extents: the reward field # - non-reward field # correlations were 0.26–0.42, $p < 6.6e-29$ for all cases)

Place field number correlation

The place field number correlation was computed as the Pearson correlation coefficient between the place field numbers of the cells in 2 environments/sessions. Silent cells were included in this calculation.

Population vector correlation

The population vector correlation analysis measured the similarity of a pair of place field representations to assess the degree of stability of the representation in the same environment across sessions and the degree of global remapping between different environments. The binary place field population vectors were determined in each 60 cm spatial bin of each environment (which could also be the same environment in 2 different sessions). Specifically, for each 60 cm bin, if a cell had a field that was present in any of the 60 1 cm bins, that cell was assigned an activity value of “1” for the population vector of that 60 cm bin, and “0” otherwise. The Pearson correlation coefficient was calculated for each pair of corresponding population vectors in the 2 environments and the average across all spatial bins was determined. Silent cells were also included for this analysis. For data from two different sessions, we used only cells which were tracked across both sessions. The first bin and last bin of the track were excluded since the animal was locked in (virtual) place at the beginning of each track at the start of each run for 5 s, and there was an identical end-of-track cue in all environments. The assessment of global remapping using corresponding locations in different virtual linear environments – where in each environment the beginnings and ends were similar (i.e., the animal was locked in virtual place at the beginning of the track at the start of each run for 5 s and there was an identical end-of-track cue) – is analogous to what is done for 2-dimensional “open field” arenas – where the corresponding borders are used as references to compare representations (e.g., 2 square shaped arenas in different rooms). However, we also assessed global remapping between different environments by correlating population vectors after the bins of one environment had been circularly shifted by 1, ..., $N-1$ bins where $N = \text{number of bins}$. As in Figure 3C, the results showed no evidence of similar representations between different environments at any shift value.

Place field shift analysis

We calculated the individual place field shift distance (i.e., the distance that a place field shifted over time within the same environment) by considering every possible pair of place fields of a given cell in 2 sessions. If cell had 2 place fields on one day and 3 place fields on another, then we calculated 6 possible shift distances. The shift distance was measured as the difference between the centers of each pair of place fields. In Figures 2B and 3B, we excluded cell pairs which had a > 300 cm shift distance and calculated the proportions in each bin (10 cm) as a function of the time gap between sessions.

Bayesian decoding

We decoded position of the animal using a standard Bayesian maximum log-likelihood approach (Davidson et al., 2009), in which we assume cells exhibit independent activity, Poisson noise, and a flat prior over the location of the animal.

$$\underset{x}{\operatorname{argmax}} \log P(x|\vec{n}) = \underset{x}{\operatorname{argmax}} \sum_i (n_i \log r_i(x)\tau - r_i(x)\tau) + C(\vec{n})$$

where x is the position of the animal, \vec{n} denotes the population vector activity, i indexes neuron identity, C depends on the population vector activity but does not depend on x (thus C is irrelevant for the maximum log-likelihood estimation), $r_i(x)$ is a calcium event rate map that was determined for each cell by discretizing the environment into 30 cm segments and averaging a binary variable defined as 1 when the calcium activity was above threshold and 0 otherwise across the times the animal was in that spatial bin, and $\tau = 1$ s. The population vector, \vec{n} , used to decode the activity was the summed activity of the binary neural activity vector over a time window of length τ preceding the present position of the animal while its running speed exceeded 5 cm/s, and the rate was scaled to match the size of the time window. The rate map and decoded activity did not come from the same sessions (i.e., the rate map from an environment on one day was used to decode the location of the animal in that same environment or another on a different day). The median decoding error (normalized by the length of the environment) was used as a measure of decoding performance, and chance performance for a decoder that guesses randomly is $1 - 1/\sqrt{2}$ times the environment size by this measure.

Place field variance explained by a model where each cell has a fixed, cell-specific propensity

To determine how much of all place field activity was explainable by the idea of a fixed propensity per cell, we did the following. We computed the observed sum of variances of the number of fields each cell had per session across 8 random reward sessions (1311

cells total from 4 mice). Then we computed the expected sum of variances assuming a fixed, Poisson propensity model: for each cell, the number of fields per session was assumed to be a Poisson random variable with parameter = the observed mean number of fields/session for that cell averaged across all 8 sessions. The sum of variances across the population was simulated 100 times. The expected sum of variances (mean of 100 simulations) was 66% of the observed sum of variances.

Place field number, across session model (Figures 4D and 4E)

Place field numbers, n , across the population in a given environment during a given session were fit using maximum likelihood to a gamma-Poisson distribution,

$$P_{\text{gamma-poisson}}(n) = \int P_{\text{poisson}}(n|\lambda)P_{\text{gamma}}(\lambda)d\lambda = \frac{\beta^\alpha}{(1+\beta)^{n+\alpha}} \frac{\Gamma(n+\alpha)}{\Gamma(\alpha)\Gamma(n+1)}$$

where Γ denotes the Gamma function, $P_{\text{poisson}}(n|\lambda) = e^{-\lambda L_{\text{env}}} (\lambda L_{\text{env}})^n / n!$ is a Poisson distribution with L_{env} representing the environment length, and the two resulting parameters α, β provide a distribution of place field propensities (λ) that are gamma distributed,

$$P_{\text{gamma}}(\lambda) = \frac{\beta^\alpha}{\Gamma(\alpha)} \lambda^{\alpha-1} e^{-\beta\lambda}$$

for each environment and session. In our model, we allowed these parameters to be different across sessions, although little variability was seen (Figure S2).

Up to this point, we have described characterizing activity within single sessions, but to characterize cross-session activity, we must connect activity across sessions. The most correlated the activity could be given these constraints would be if the cell propensities had their ordering preserved (i.e., for every pair of neurons m, n and sessions s, t , the propensity relationship $\lambda_s^m < \lambda_s^n$ implies that $\lambda_t^m < \lambda_t^n$). If we consider the cumulative distribution function variables, X_s, X_t , the joint distribution describing propensities for a cell in two different sessions under this order-preserving condition would be $P(X_s, X_t) = \delta(X_s - X_t)$. The full joint distribution of place field numbers for all cells in both environments is then uniquely determined:

$$P(n_s, n_t) = \int_0^\infty \int_0^\infty P(n_s|\lambda_s)P(n_t|\lambda_t)P(\lambda_s, \lambda_t)d\lambda_s d\lambda_t = \int_0^1 \int_0^1 P(n_s|\lambda_s(X_s))P(n_t|\lambda_t(X_t))P(X_s, X_t)dX_s dX_t$$

where $\lambda_s(X_s)$ is the inverse CDF. Note that the joint distribution in propensity space may be written:

$$P(\lambda_s, \lambda_t) = \delta(\lambda_s - X_s^{-1}[X_t(\lambda_t)])P(\lambda_t)$$

with $X_s(\lambda_t)$ denoting the CDF in session t and X_s^{-1} denoting the inverse CDF in session s . With this joint distribution, we sampled the predicted number distributions 500 times to measure the correlations and their variability (plotted using 2 standard deviations in each direction) due to neuronal sample size.

Place field number, reward field number model (Figure 6)

Because we observed significant correlations between reward field numbers and non-reward place field numbers, we sought to determine whether these correlations could be explained by the gamma-distributed propensity that matched the observed place activity. We modeled the non-reward place activity using a gamma-Poisson distribution, and fit a gamma distribution (2 parameters) to the non-reward place field activity observed during the session with no reference to reward activity. Because it is observed that overall population activity increases in reward contexts by a significant amount, we modeled the reward field propensity, λ_r , as a constant gain factor, G , multiplying the propensity of the cell in a non-reward place context:

$$P_{\text{reward}}(\lambda_r) = \frac{(\beta/G)^\alpha}{\Gamma(\alpha)} \lambda_r^{\alpha-1} e^{-\beta\lambda_r/G}$$

The probability of having no reward field in some region of space declines exponentially for a spatially Poisson process, and so the probability of having a reward field in a single reward area is:

$$P_{\text{reward field}}(\text{reward field}|\lambda_r) = 1 - e^{-\lambda_r L_{\text{reward}}}$$

where L_{reward} is the length of the reward area. If we additionally assume that each reward area has statistically the same properties, then the distribution over reward field number, n_r , conditioned on reward propensity will be a binomial distribution:

$$P_{\text{binomial}}(n_r|\lambda_r) = \binom{R_{\text{total}}}{n_r} (1 - e^{-\lambda_r L_{\text{reward}}})^{n_r} (e^{-\lambda_r L_{\text{reward}}})^{R_{\text{total}} - n_r}$$

where R_{total} is the total number of reward areas in the environment. The full distribution describing reward field numbers can be computed, giving rise to a gamma-binomial distribution over reward field numbers:

$$P_{\text{gamma-binomial}}(n_r) = \int P_{\text{binomial}}(n_r | \lambda_r) P_{\text{reward}}(\lambda_r) d\lambda_r = \binom{R_{total}}{n_r} \sum_{k=0}^{n_r} \binom{n_r}{k} (-1)^k \left(1 + \frac{G(R_{total} - n_r + k)}{\beta}\right)^{-\alpha}$$

We fit G using maximum likelihood to the marginal distribution of reward activity with the gamma parameters fixed to those describing the non-reward place activity. To fully describe the joint distribution of non-reward place and reward activity, the joint distribution must be specified. Given that we observed strong correlations in non-reward place and reward activity, we began by using an analogous order-preserving hypothesis, $P(X_p, X_r) = \delta(X_p - X_r)$, where X_p and X_r are variables representing place and reward propensity, respectively, in CDF space. Using this constant gain model, we observed a very good match for each session for two animals, but two animals had non-reward field-reward field correlations lower than that predicted by the model. To account for these differences, we hypothesized that there may be additional variability, which would result in a broadening of the joint distribution beyond a delta function. To loosen this constraint, we used a copula, a mathematical tool guaranteed to match marginal distributions while varying the underlying joint distribution (Nelsen, 1999). A copula defines a multi-dimensional distribution with marginal distributions that are uniform distributions on the interval [0, 1]. These uniform marginal distributions may be easily mapped to any marginal distribution using its inverse CDF. The probability density may be written:

$$P(\lambda_1, \lambda_2) = P(\lambda_1) c(X_1(\lambda_1), X_2(\lambda_2)) P(\lambda_2)$$

where $P(\lambda_i)$ describes each marginal distribution, $X_i(\lambda_i)$ is the CDF evaluated at λ_i , and c is the copula density. We chose simple copulas whose single continuous parameter allows the joint distribution to vary from a delta function (perfect order preserving) to a uniform distribution (no correlation between reward and non-reward place activity). After testing the Clayton, Frank, and Gumbel copulas, we observed that the Clayton copula best matched the data (as assessed by the Jensen-Shannon divergence):

$$C_{\text{Clayton}}(X_p, X_r; \theta) = \left[\max\left(X_p^{-\theta} + X_r^{-\theta} - 1, 0\right) \right]^{-1/\theta}$$

where the copula parameter, θ , was chosen to match the correlation observed from the data (after fixing the gain and gamma distribution parameters that define the marginal distributions). In sum, this model contains four parameters: two representing the gamma distribution describing non-reward place activity, one representing the reward-based gain, and one representing the degree of correlation between the reward and non-reward place activity. The model makes predictions about the full joint distribution, which we simulated and compared to the experimentally observed sessions using the Jensen-Shannon divergence:

$$D_{JS}(P_{model}, P_{data}) = \frac{1}{2} \left[D_{KL}\left(P_{model}, \frac{P_{model} + P_{data}}{2}\right) + D_{KL}\left(P_{data}, \frac{P_{model} + P_{data}}{2}\right) \right]$$

where D_{KL} denotes the Kullback-Leibler divergence between two models, which is a measure of how distinguishable one probability distribution is from another. The Jensen-Shannon divergence is a measure of how distinct two distributions are from one another, and is preferable to the Kullback-Leibler divergence when one distribution has support over many more outcomes (i.e., a model which predicts small but finite probabilities for unlikely events) than are observed in the other (i.e., data) due to finite sampling. Additionally, we compared the Jensen-Shannon divergence between the observed and modeled results for an alternative model that did not assume a constant gain, but instead allowed the reward propensity to be a nonlinear function of the non-reward field propensity. Specifically, we allowed $\lambda_r = G(\lambda_p)\lambda_p$, where $G(\lambda) = G_0(1 + e^{-\lambda/\bar{\lambda}})$, and fit the resulting parameters, G_0 , k , and $\bar{\lambda}$, using a maximum-likelihood framework to the full observed joint distribution, $P_{data}(n_p, n_r)$ after fixing the gamma distribution parameters for non-reward place activity (5 total parameters). We also evaluated a power law distribution for the gain with the same number of parameters, but the exponential form performed better in terms of matched correlations and the Jensen-Shannon divergence. The results showed that the constant gain model with Clayton copula was a better match to the data (measured by the Jensen-Shannon divergence) than this exponential gain model that notably had more parameters and was fit to match the full joint distribution observed in the data (Figure 6).

Place field number, spatial correlation (Figure 7D)

To analyze whether nearby neurons had similar numbers of place fields, we computed the correlation in field numbers of pairs of neurons whose centers were < 25 μm apart. There was a small but significant correlation in 2 of 4 mice (mouse 1: $r = 0.18$, $p < 0.001$, 737 pairs of cells; mouse 2: $r = 0.035$, $p = 0.49$, 380 pairs; mouse 3: $r = 0.089$, $p = 0.015$, 753 pairs; mouse 4: 0.14 , $p = 0.061$, 171 pairs). However, this correlation disappeared when we controlled for the moderate gradients in propensity across the superficial-deep (Mizuseki et al., 2011; Danielson et al., 2016) and proximal-distal axes (Henriksen et al., 2010) of dorsal CA1. Specifically, we first applied low-pass spatial filtering by subtracting from each cell's field number the mean field number within an 80 μm radius, then computed the correlation between pairs of neurons < 25 μm apart using the corrected field numbers. The correlation was

not significant in any animal (Figure 7D), indicating large fluctuations (see Figures 7A–7C and S3A) in propensity from neuron to neuron riding on top of these anatomical gradients, i.e., propensity is organized in a largely salt-and-pepper manner.

Intracellular recording analysis

We analyzed 21 CA1 pyramidal cells that were intracellularly recorded while the mice ran in familiar environments (28 sessions total). The subthreshold V_m trace was determined from the raw V_m trace as described previously (Epsztein et al., 2011; Lee et al., 2012; Cohen et al., 2017). Briefly, all APs and any parts of the raw V_m trace that are directly attributable to the somatic APs themselves (e.g., after-depolarizations) were removed. This included removing the entirety of the slow, putatively calcium-based depolarization that often follows a burst of APs, which also removes the entirety of any intracellular complex spikes. The remaining trace was linearly interpolated across the resulting gaps to yield the subthreshold V_m trace. We then calculated the mean subthreshold V_m as a function of location every 4 cm using a 12 cm wide boxcar window for each lap, then averaged the results from each lap over the session. From this session-average V_m as a function of location, we found the location of the maximum V_m , then found additional peak V_m locations as follows: we excluded ± 4 bins (each bin is 4 cm) centered at the maximum peak location, then found the peak in each successive group of 8 bins on each side, and if a peak was < 4 bins away from a previously determined peak in another group, we found the highest value in the group ≥ 4 bins away from the peak in that other group and assigned that to be the peak. The peaks found for 2 example sessions are shown in Figure 7F and for all 28 sessions in Figure S6A. The baseline V_m was computed as the mean of the lowest 10% of bins of the session-averaged V_m (Epsztein et al., 2011; Lee et al., 2012; Cohen et al., 2017). The amplitudes of the peaks were computed as the peak V_m – the session's baseline V_m , then the data from each cell with more than one session were combined as follows: the peaks from each session were grouped together and the overall baseline for the cell was computed as the average of the baselines across the sessions. For the reward area, we included the 3 bins before and 10 bins after the 3 bins where reward was consistently delivered, for a total of 16 bins. The AP threshold for a cell was determined as described previously (Epsztein et al., 2011; Cohen et al., 2017). For cells with more than one session, the mean of the thresholds determined for each session was used. For cells which did not have a threshold value for any of the included familiar environment sessions (e.g., because the cell was silent in those sessions), the threshold of the cell in a novel environment session was used, since it was shown that thresholds do not differ on average in novel and familiar environments (Cohen et al., 2017). Finally, if a cell did not have a threshold value in any of its sessions (e.g., if it was silent in all sessions), the threshold determined from current step pulses (based on 10 V/s crossing of first evoked spike) before any virtual environment was displayed was used.

Probabilistic simulation of field propensity distribution based on intracellular data

Our experimental data showed that peak V_m amplitudes varied between cells (Figures 7G and S6A–S6C) as well as within a cell across locations (Figure S6A). For this simulation, we created two distributions from the data to represent these features. Because cells with larger amplitude peaks tended to have smaller AP threshold – baseline (as in “AP threshold minus baseline”) values (Figure S6E), to integrate the data across cells we first scaled each cell's V_m values to its baseline and threshold such that 0 represented the baseline value and 1 the threshold value. The peak amplitudes of each cell were thus scaled. The distribution of the mean (scaled) peak amplitude per cell across different cells was skewed similarly to Figure S6B and was fit with a gamma distribution (Figure S6G, left). We used this (“mean peak amplitude”) distribution (Figure S6G, left) to simulate the different average peak amplitudes across different cells, which relates to propensity. We then constructed a single distribution to represent the variation of peak amplitudes within a cell by normalizing the peak amplitudes within each cell by dividing them by the mean peak amplitude of that cell and pooling the data across all 21 cells (Figure S6G, right). This distribution also displayed a skewed shape and was fit with a log-normal distribution. We used this (“peak amplitude spatial variation”) distribution (Figure S6G, right) to simulate the different peak amplitudes in different spatial locations for each given cell. We simulated cellular activity of 1000 cells in 3 large environments each with 4 consistently rewarded locations, by simulating (per environment) 60 peak amplitudes per cell (56 non-reward and 4 reward peak amplitudes; note that the average running speed of the animals in the intracellular experiments was ~ 16 cm/s and in the imaging experiments 28.6 ± 0.1 cm/s, mean \pm s.e.m., therefore one peak per 8 bins = 32 cm in the intracellular data scales in time to approximately one peak per 60 cm in the imaging experiments, i.e., ~ 60 peaks per 40 m). Each cell was assigned a mean peak amplitude randomly drawn from the mean peak amplitude distribution (Figure S6G, left). Then for each cell, the 60 individual peak amplitudes of the cell per environment were determined by randomly drawing 60 times from the peak amplitude spatial variation distribution (Figure S6G, right) and multiplying by the cell's mean peak amplitude:

$$\text{peak}_i = (\text{mean peak amplitude of the cell}) \times (\text{peak amplitude spatial variation value } i)$$

Because we computed the mean V_m traces over 12 cm windows (representing ~ 0.75 s of running), any theta or gamma oscillations were averaged out before calculating the peak V_m amplitudes. To account for this, we plotted the standard deviation of V_m as a function of the mean subthreshold V_m in each bin (before averaging across laps) and used the linear fit (note V_m values below baseline were excluded) to simulate the amount that oscillations would help a given peak cross threshold. That is:

$$\text{SD}_i = (\text{peak}_i) \times (\text{slope of SD versus mean } V_m) + (\text{SD offset})$$

and:

$$\text{peak}_{i,\text{adjusted}} = \text{peak}_i + 2 \times \text{SD}_i$$

For the peak amplitude in a rewarded area, we multiplied peak_i by the linear regression slope of the mean V_m in rewarded areas versus the mean of V_m in non-reward areas (i.e., 1.34, Figures 7H and S6F). Place fields or reward fields were determined if $\text{peak}_{i,\text{adjusted}}$ was ≥ 1 (i.e., the AP threshold value since we had scaled values such that baseline = 0 and threshold = 1). The resulting field number distributions in rewarded and non-rewarded areas (Figures 7I and S6H) are similar to those observed in the imaging data. A nearly identical simulation was also performed, where in this case the baseline, threshold, and mean peak V_m values were drawn independently from their separate distributions (Figures S6B, S6D, and S6E) in the data (i.e., no account was taken of the cell these 3 values came from, unlike in the above simulation in which cells with larger mean peak V_m amplitudes tended to have smaller threshold – baseline values) and V_m values were not scaled to each cell's threshold – baseline. Interestingly, the field number distributions in this “independent” simulation differed from the observed imaging distributions by having a subset of cells that was active in every location, rewarded and not. Another simulation in which the baseline was not considered, but the relevant feature was threshold – peak amplitude, also resulted in field distributions that differed from the observed distributions, including by having a substantial number of cells that were active in most locations. That the threshold – baseline scaled simulation matched the imaging data much better than these other simulations further suggests that the amplitude of inputs (as measured at the soma) and other cellular properties such as threshold and baseline are linked, possibly by a single factor like excitability.

Biophysical model of field propensity distribution centered on INaP differences and fit to intracellular data

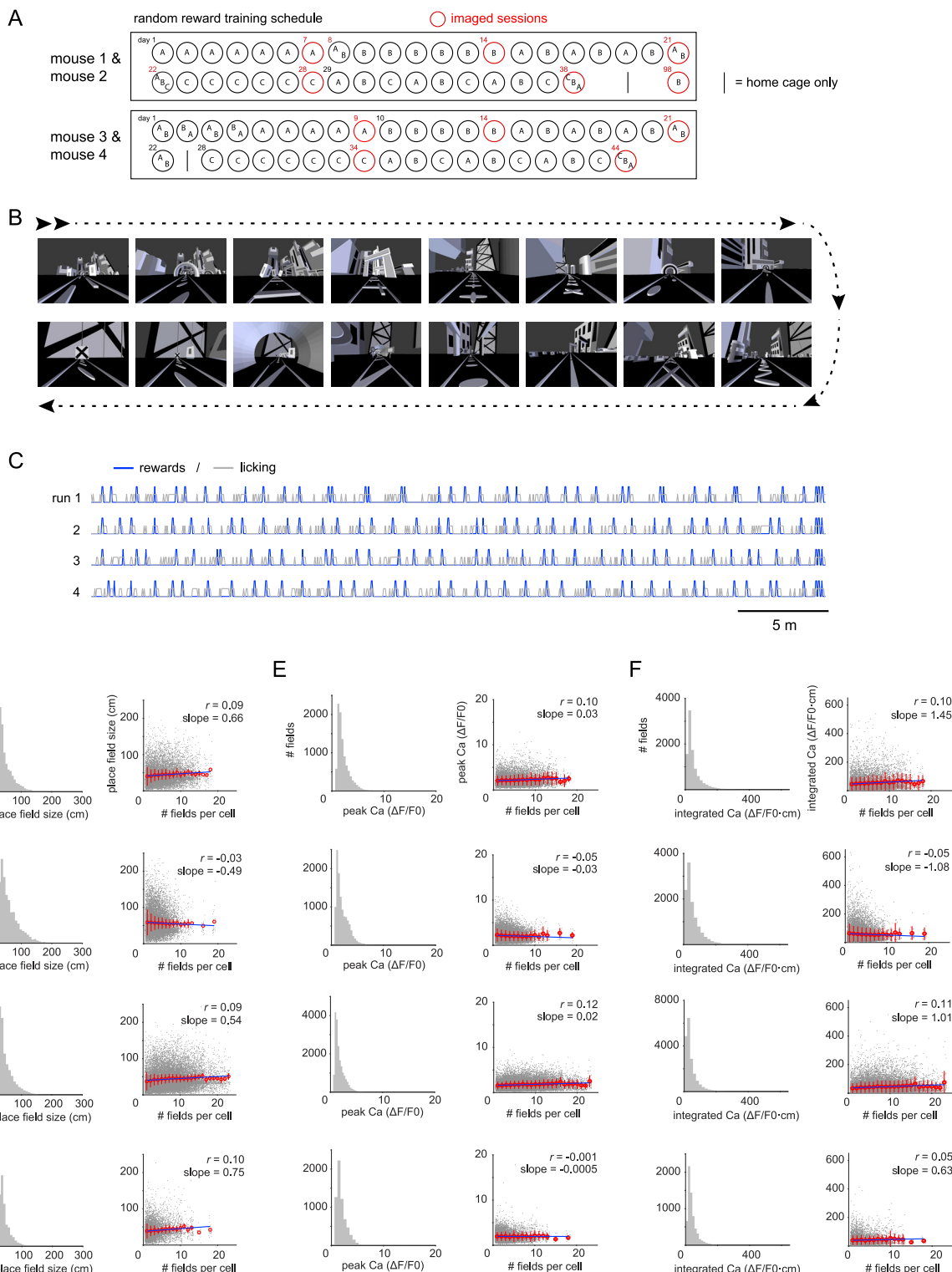
To simulate intracellular V_m traces, we used DynaSim (Sherfey et al., 2018). We simulated a simple, single-compartment Hodgkin-Huxley-type model with 4 conductances. We fixed the values of 3 conductances: fast Na^+ channel conductance = 111 mS/cm² with reversal potential = +58 mV, fast K^+ channel conductance = 2.0 mS/cm² with reversal potential = -77 mV, and leak conductance = 0.713 mS/cm² with reversal potential = -71 mV (based on values from Hodgkin and Huxley [1952] and Golomb et al. [2006]). Persistent Na^+ conductance (G_{iNaP}) ranged from 0.0 to 6.0 mS/cm² with reversal potential = +58 mV (compare to mean value of 2.2 mS/cm² for L5 pyramidal neurons in the PFC) (Durstewitz et al., 2000). We used the parameters for channel kinetics in the DynaSim library without modification. All V_m simulations started with $V_m = -65$ mV and had fixed time step $dt = 0.05$ ms. We adjusted the resting V_m by applying a +1.50 mV DC offset to the input.

Our approach was to simulate each cell's activity across the environment as a series of inputs of varying amplitude (representing variations in input as a function of location) that would yield output V_m peaks of various amplitudes, some of which would cross threshold to yield place fields in those locations (note that here the threshold was not a parameter, but was instead a result determined by DynaSim based on the conductances and the dynamics of the simulation). Cells with higher G_{iNaP} would amplify inputs more and thus have larger amplitude output V_m peaks and more place fields. We fit the model to the intracellularly recorded data by determining two distributions. The first is the variation in input amplitude as a function of location, which we assumed to be the same for all cells. The second is the distribution of G_{iNaP} across cells. To determine these distributions, we started by using DynaSim to produce subthreshold input-output V_m amplitude curves as follows. We generated output V_m traces using input in the form of a raised cosine of various amplitudes (shape: $1 + \cos(\theta)$, $-\pi \leq \theta \leq \pi$ over a 2 s time window, input amplitude: 0 to 5.0 mV with 0.1 mV increment) with a single G_{iNaP} value. This 2 s raised cosine matched the average time between adjacent V_m peaks in the intracellular data (average inter-peak spacing = 8 bins = 32 cm, running speed ~16 cm/s). We repeated this for different G_{iNaP} values (0.0 to 6.0 mS/cm² with 0.5 mS/cm² increment). For each G_{iNaP} value, we plotted the peak output V_m value as a function of the input amplitude. We excluded cases where an AP was generated and we fit the remaining data points to make functions to estimate the peak sub-threshold output for any given input and G_{iNaP} value within the range 0.0–6.0 mS/cm² (Figure S7B1), including what the underlying subthreshold peak V_m would have been if the APs had not occurred for suprathreshold input values (this was necessary because, unlike real intracellular data in which the threshold of successive spikes increases and thus the increases in underlying depolarization during a series of spikes can be estimated, the simplified cell model we use exhibits a constant threshold). To determine the distribution of input amplitudes, we noted that the 15/21 cells (~70% of cells) with the lowest mean peak amplitudes yielded a distribution of normalized individual peak amplitudes (normalized by each cell's mean peak amplitude) that was well-described as a Gaussian (Figure S7A3), while the 6/21 cells (~30% of cells) with the highest mean peak amplitudes yielded a skewed distribution of normalized individual peak amplitudes (Figure S7A4). We reasoned that the cells with lower mean peak amplitudes represented cells in which none of the inputs were amplified by G_{iNaP} much, and thus that the distribution of input amplitudes would be similar to that of the output peaks, i.e., Gaussian. The skewed distribution of peaks for the cells with higher mean peak amplitudes would be the result of the same Gaussian distribution of inputs, but with the larger inputs amplified more by the higher values of G_{iNaP} . A Gaussian distribution of inputs with mean \pm s.d. of 1.0 ± 0.4 mV produced a good match to the intracellular data (Figure S7B2). To determine the distribution of G_{iNaP} across cells that best matched the observed intracellular data (Figure S7C), we did the following. Using the input-output functions from above, we simulated 601 groups of cells with different G_{iNaP} values (from 0.0 to 6.0 mS/cm² in increments of 0.01 mS/cm²). To match the average number of V_m peaks per cell in the intracellular data (i.e., 8), 8 inputs were given to each cell, with the inputs randomly drawn from the Gaussian input distribution. For each of the 601 G_{iNaP} values, we simulated the output of 100 cells of 8 random inputs each. We then searched for the set of cells based on their G_{iNaP} values that best matched 4 experimentally measured distributions: the distribution of mean peak amplitude (i.e., the mean of 8 output peaks per cell), which was fit with

a gamma (Figure S7A1); the normalized peak amplitude distribution of all peaks across all cells (i.e., for each cell, the 8 output peaks were normalized by the mean of the output peaks of that cell, then pooled across all cells), which was fit with a log-normal (Figure S7A2); the normalized peak amplitude distribution of the 70% of cells with lowest mean peak amplitude, which was fit with a Gaussian (Figure S7A3); and the normalized peak amplitude distribution of the 30% of cells with highest mean peak amplitude, which was fit with a log-normal (Figure S7A4). We began with a simulated set of 20 groups of 100 cells (i.e., 20 G_iNaP values) and compared the fitting parameters for each of the 4 distributions between the simulated data and experimental data. We repeated this process for random sets of 20 groups of cells and kept any set for which the difference in each fitting parameter to the experimental data was < 30% until we found 100 such sets. Among these 100 sets, we kept the 10 sets with the smallest summed difference in fit parameters and merged them to yield a distribution of G_iNaP values. We iteratively improved the fitting by repeating this process with sets of 40 groups of cells whose G_iNaP values were randomly drawn not from a uniform distribution between 0.0 and 6.0 mS/cm², but from the G_iNaP distribution from the previous result from sets of 20 groups of cells. We repeated this process with 80, 160, and 320 groups of cells. We verified that our final G_iNaP distribution (Figure S7C) (320 groups of 100 cells, 8 input amplitudes drawn from the Gaussian input distribution for each cell) produced a good match to the experimental data (Figure S7D1–4; compare to intracellular data in Figure S7A1–4; note that it was not possible to perfectly match all 4 distributions simultaneously; also note that, because we only used the minimum number of conductances plus G_iNaP in our model and we were most interested in matching the shapes of the 4 distributions, we allowed the distribution of absolute mean peak amplitudes of the simulated data to be shifted, and for this we shifted the simulated distribution by –0.7 mV before assessing the fit during each iteration – i.e., compare Figures S7A1 and S7D1; we did not shift any values for the distributions in Figure S7D2–4 and the comparison to Figure S7A2–4).

Based on this G_iNaP distribution, we simulated 700 cells with sixty 2 s-long raised cosine inputs (same as above) per cell (56 for non-rewarded and 4 for rewarded areas), with the input amplitudes drawn from the same Gaussian distribution (mean ± s.d. = 1.0 ± 0.4 mV), as well as the +1.50 mV DC offset. DynaSim was used to simulate the output V_m and a place (or reward) field was assigned whenever an input produced ≥ 1 AP (Figure S7E). For rewarded areas, we first increased the input amplitude by a constant amount (mirroring the model assumption that the distribution of inputs to all cells is the same, Figure S7B2), 0.35 mV, which produced a multiplicative relationship between reward versus non-reward output (Figure S7E7), as observed in the intracellular data (Figure 7H). The simulation also resulted in a correlation of mean peak (output) V_m amplitude with baseline, an anticorrelation of mean peak V_m amplitude with threshold – baseline, and a shape of distribution of baseline values as observed in the intracellular data (compare Figure S7E4–6 to Figure S6D and S6E). (Note that in our biophysical modeling we did not attempt to quantitatively match the absolute membrane potential values in the intracellular data. Rather, we chose a simplified model with the minimum number of conductances to explore potential key mechanisms, and our goal was to match the shapes and relationships of all the observed distributions as closely as possible while having the absolute magnitudes be reasonably similar to the observed values.) Because of the observed correlation between mean peak V_m amplitude and baseline, we also considered a variation of the biophysical model to explore the following possibility – that differences in baseline V_m caused by differences in DC input to different cells, instead of differences in G_iNaP between cells, could result in differences in propensity. We simulated 700 cells that all had the same G_iNaP value of 2.5 mS/cm² (similar to measured values) (Durstewitz et al., 2000) and the same Gaussian distribution of inputs (mean ± s.d. of 1.0 ± 0.4 mV), but DC offset values of 0.0–3.0 mV added to the input (noting that going much above 3.0 mV caused cells to always cross threshold). The distribution of DC offsets across cells needed to best match the intracellular data (Figure S7A1–4) was determined and used for the simulation. For rewarded areas, we increased the input amplitude by a constant amount, as before. The results produced skewed distributions of non-reward and reward field numbers (Figure S7F1) that appeared less similar to the observed distributions than the variable G_iNaP simulation and, furthermore, the distribution of baseline values was significantly different than the observed intracellular data (compare Figures S7F6 to S6D, right).

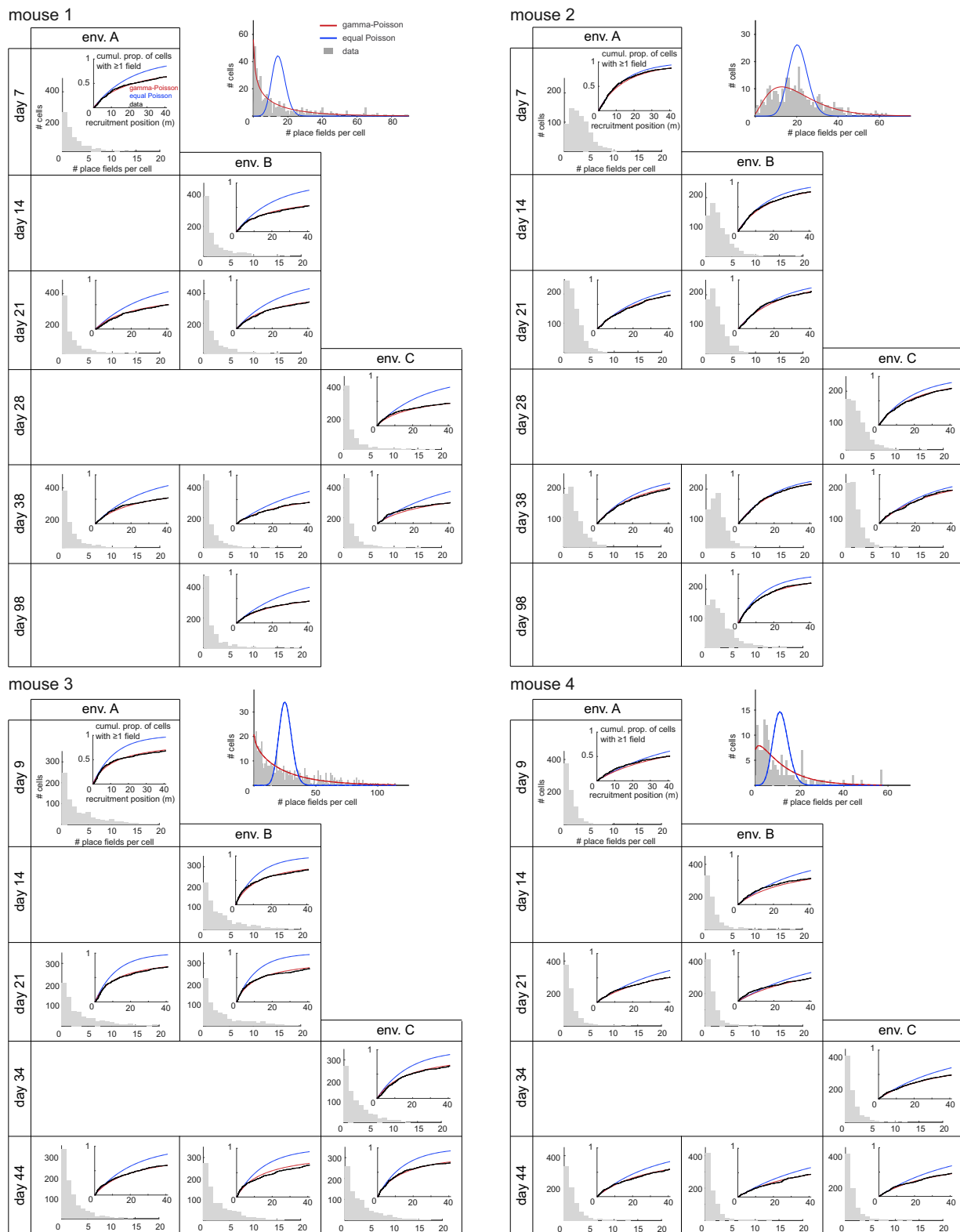
Supplemental Figures



(legend on next page)

Figure S1. Training Schedule, Example Environment, and Behavior in Virtual Environments and Relationship between Propensity and Basic Place Field Properties, Related to Figure 1

(A) Daily training schedule for mouse 1 and mouse 2 (top), and mouse 3 and mouse 4 (bottom). A, B, C represent the 3 environments explored by each animal (selected from 4 environments), where A represents the first environment explored by each animal regardless of its identity. Red circles indicate the 9 (mouse 1 and 2) and 8 (mouse 3 and 4) calcium imaging sessions used for random reward condition analyses (mouse 1 and 2 days 8 and 22 were also used for the Δ1 day analysis in Figures 2B–2D, 4A, and 4B). (B) Sequential view along the running path for one of the 4 virtual environments. (C) Mouse licking behavior in each lap. Blue lines indicate randomly delivered water rewards and gray lines indicate mouse licking. (D–F) These results show that several basic features of individual place fields, such as the mean width, peak activity level, and integrated magnitude of a field, were generally similar whether the field arose from a cell with low or high propensity. (D) Distribution of place field size (left). Place field size (44 ± 25 cm, 57 ± 32 cm, 44 ± 26 cm, 40 ± 21 cm in each mouse, mean \pm s.d.) was only weakly correlated with the number of place fields of the corresponding cell (right). Average place field size for cells with a given number of place fields (red, mean \pm s.e.m.). While the correlation was significant ($p < 3e-5$ for each animal), the correlation was weak (ranging from -0.03 to 0.10) and the slope was small and of either sign (-0.49 to 0.75 , e.g., the mean field width differs by ~ 5 cm for cells with 10 fields versus 1 field, compared to an overall mean width of ~ 45 cm). (E) Similar to (D) except for peak calcium fluorescence ($\Delta F/F_0$) of each place field. Peak calcium fluorescence was significantly (for each animal except mouse 4), but only weakly, correlated with the number of place fields of the corresponding cell, and the slope was small and of either sign (right). (F) Similar to (D) except for integrated calcium fluorescence ($\Delta F/F_0 \cdot \text{cm}$) of each place field. Integrated calcium fluorescence was significantly (for each animal), but only weakly, correlated with the number of place fields of the corresponding cell, and the slope was small and of either sign (right).



(legend on next page)

Figure S2. The Number of Place Fields of Each Cell In Different Virtual Environments on Different Days Is Well Described by the Gamma-Poisson Model, Related to Figure 1

Each panel shows the distribution of the number of place fields of each cell in each (random reward) session for the 4 mice. Each mouse had somewhat different distributions, but across the sessions of a given mouse the distribution was preserved over time and environments (distributions on days 7, 14, and 28 for mouse 1 and 2, and 9, 14, and 34 for mouse 3 and 4 were used for these comparisons, K-S test, $p > 0.15$). Inset in each panel shows the cumulative recruitment of cells along the track (i.e., a cell is defined as recruited by position x if it has a place field between 0 and that position) (black) with the prediction from the equal Poisson model (blue) and the gamma-Poisson model (red). This shows good agreement with the gamma-Poisson model. For each cell with ≥ 6 fields in a session, the distribution of field locations and distribution of inter-field intervals did not differ from the spatial Poisson model predictions of uniform and exponential, respectively (K-S test for uniform distribution, Anderson-Darling test for exponential distribution after 30 cm subtracted from each inter-field interval to account for gap parameter in determining place fields, each test yielded 0/2132 cells with $p < 0.05$, adjusted for false discovery rate, $q = 0.5$), consistent with the fields of each cell being distributed randomly in space, as shown previously (Rich et al., 2014). Top right plot for each animal shows the distribution of the total number of place fields across all (random reward) sessions per cell (sum over the 8 or 9 sessions shown in the bottom left panels).

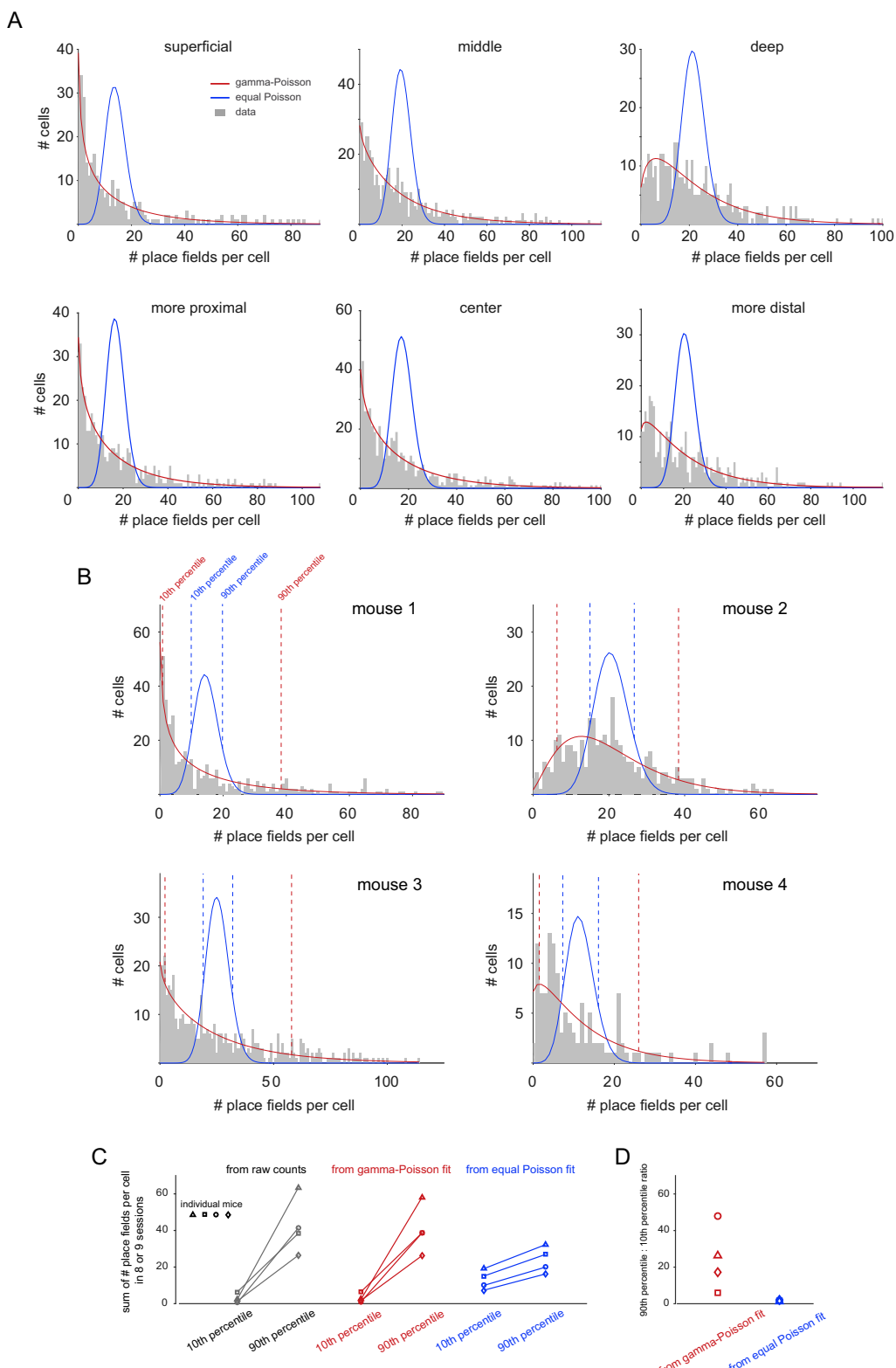


Figure S3. The Distribution of the Number of Place Fields Per Cell Varies by an Order of Magnitude across the Population, Related to Figure 1
 (A) The distribution of the total number of place fields across all (random reward) sessions per cell for subpopulations of cells along the superficial-deep (top) or proximal-distal axes (bottom) (pooled data from the 4 mice). Superficial-deep location of each cell was estimated from a z stack of images taken above and below

(legend continued on next page)

the imaging plane. The cells from 0%–35% of the way from the superficial to deep edges of the pyramidal cell layer were included in the superficial group, and from 65%–100% in the deep group. The cells from 40%–60% were included in the middle group. The different sizes of the ranges were used to balance the number of cells in each group. For the proximal-distal axis, we divided our imaging plane into 3 regions: 1/3 of anterior lateral region as proximal, 1/3 of posterior medial region as distal, and the rest 1/3 as center (our imaging plane is the left hemisphere dorsal CA1). Equal Poisson (blue) and gamma-Poisson (red) probability density functions were fit in each panel. The large deviation from the equal Poisson fit demonstrates that cells do not have the same field propensity. (B) The distribution of the total number of place fields across all (random reward) sessions per cell (gray), with equal (blue) and gamma-Poisson (red) fit (same as in Figure S2). Dotted lines indicate 10th and 90th percentile of each fit of corresponding color. (C) Comparison of 10th and 90th percentile of total number of place fields across all (random reward) sessions for each animal (unique symbol per mouse). (D) The ratio of 90th:10th percentile propensity from gamma-Poisson (red) and equal Poisson (blue) fit.

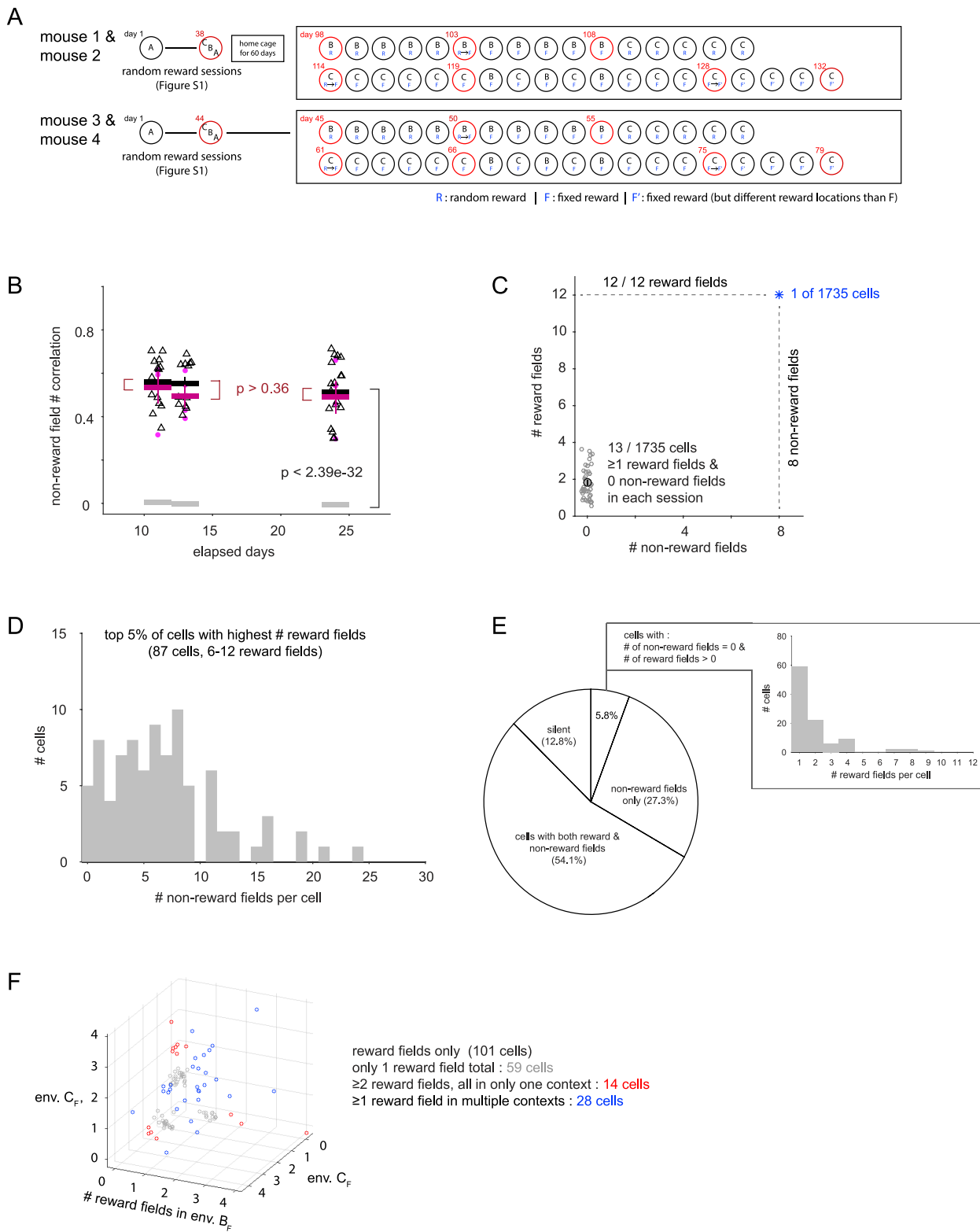


Figure S4. Reward and Non-reward Activity in Fixed Reward Location Experiments, Related to Figure 5

(A) Daily training schedule for mouse 1 and mouse 2 (top), and mouse 3 and mouse 4 (bottom). Red circles indicate the calcium imaging sessions. CF and CF' correspond to the same environment but with a different set of 4 fixed reward locations. Note that the set of 4 fixed reward locations in BF is also distinct from both

(legend continued on next page)

CF and CF'. (B) The number of place fields per cell in non-rewarded regions of the environments in the fixed reward sessions were correlated across environments and time (magenta: mean \pm s.e.m., magenta filled circles: individual session pairs; gray: shuffled data) and not different from the correlations of field numbers in the random reward sessions (black: mean \pm s.e.m., black open triangles: individual session pairs). (C-F) Cells with reward-related activity have a spatial component as opposed to being only responsive to reward. Cell data was pooled across the 3 fixed reward sessions of the 4 mice (BF: day 108 for mouse 1 and 2, day 55 for mouse 3 and 4, CF: day 119 for mouse 1 and 2, day 66 for mouse 3 and 4, CF': day 132 for mouse 1 and 2, day 79 for mouse 3 and 4), using only those cells tracked across all 3 sessions: 1735 cells total. (C) 13 of 1735 cells had at least 1 reward field in every fixed reward session and no non-reward fields. In each environment (13×3 sessions, bottom left), these cells generally had reward fields in only a subset of the 4 rewarded locations. Only 1 cell had reward fields in all 12 rewarded locations across all 3 sessions, and it also had 8 non-reward fields. (D) The ~5% of cells with the largest total number of reward fields generally each had several non-reward fields. (E) The proportion of the 1735 cells in each of 4 categories (cells with both reward and non-reward fields, non-reward fields only, reward fields only, and those with no fields). 5.8% of cells (101/1735) had only reward fields, and these cells generally had fields in only a few of the 12 rewarded locations (box). 90.3% of cells (i.e., $54.1\% / (54.1\% + 5.8\%)$) that had a reward field also had ≥ 1 non-reward field. (F) To search for context-specific reward cells (i.e., cells with fields in every rewarded location in ≥ 1 environmental context and 0 reward fields in the other contexts, that is, either 4 or 0 fields in the 4 rewarded locations in each of the 3 fixed reward configurations), we plotted the number of reward fields in each of the 3 environments for the 101 cells (5.8% of cells) with reward fields only. These cells generally had fields in only a subset of the 4 rewarded locations in any given environment.

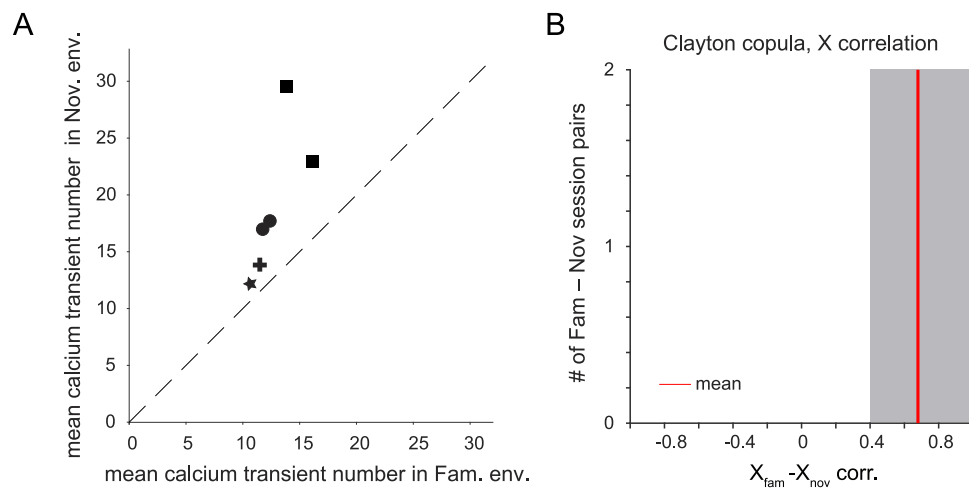


Figure S5. Increased Calcium Transient Activity in Environment When Novel versus Familiar Can Be Explained by Copula-Modified Constant Gain Model, Related to Figure 6

(A) Mean number of calcium transients per cell in first (novel) session in an environment versus a session when it was very familiar (≥ 15 previous sessions in that environment, 6 such pairs total, at least 1 from each mouse, random reward sessions only, unique symbol per mouse). (B) Correlations of copula models fit to each familiar and novel pair (value of 1 implies perfect order preservation). See Figures 6G and 6H, which show the same result in terms of place fields.

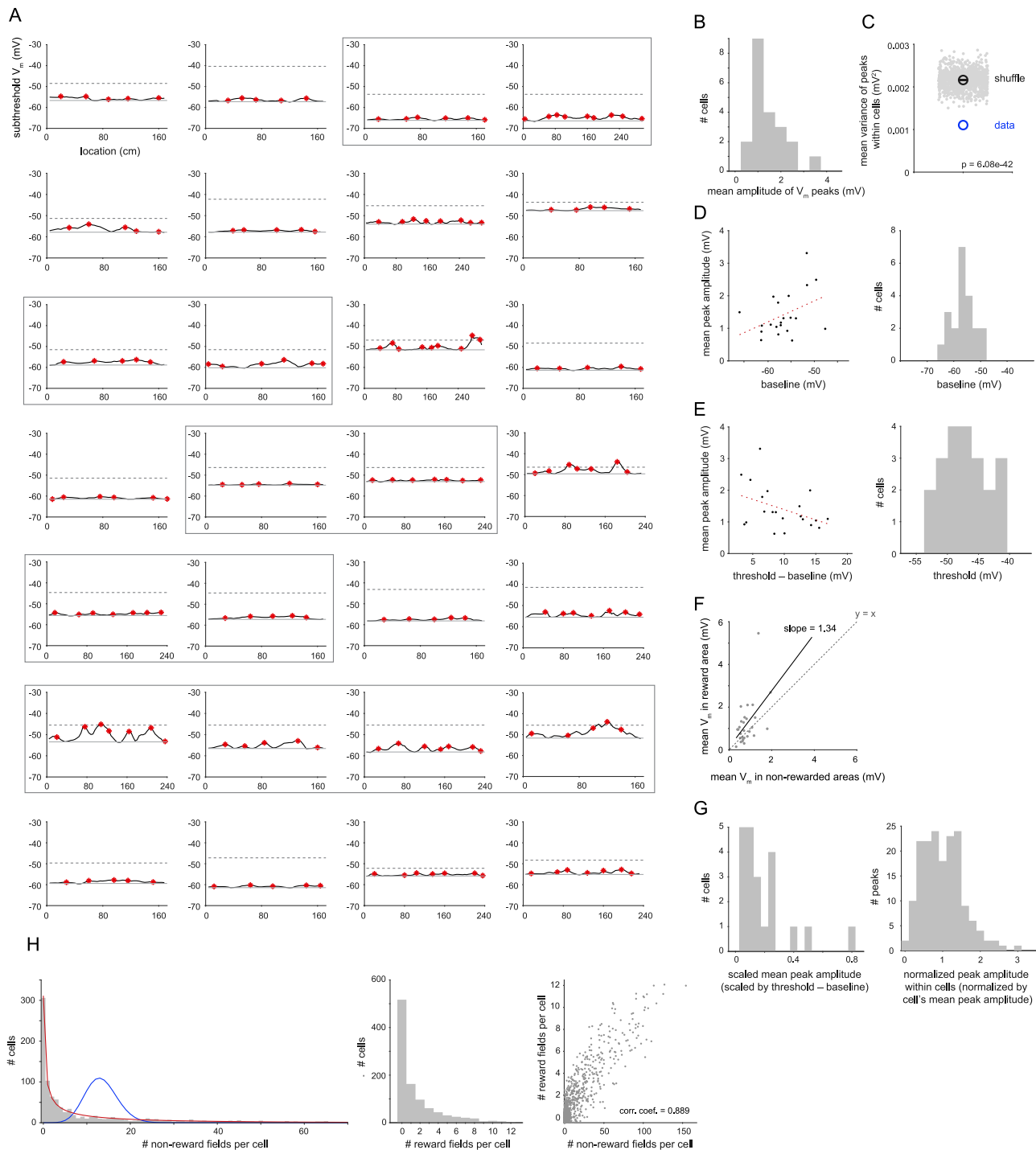
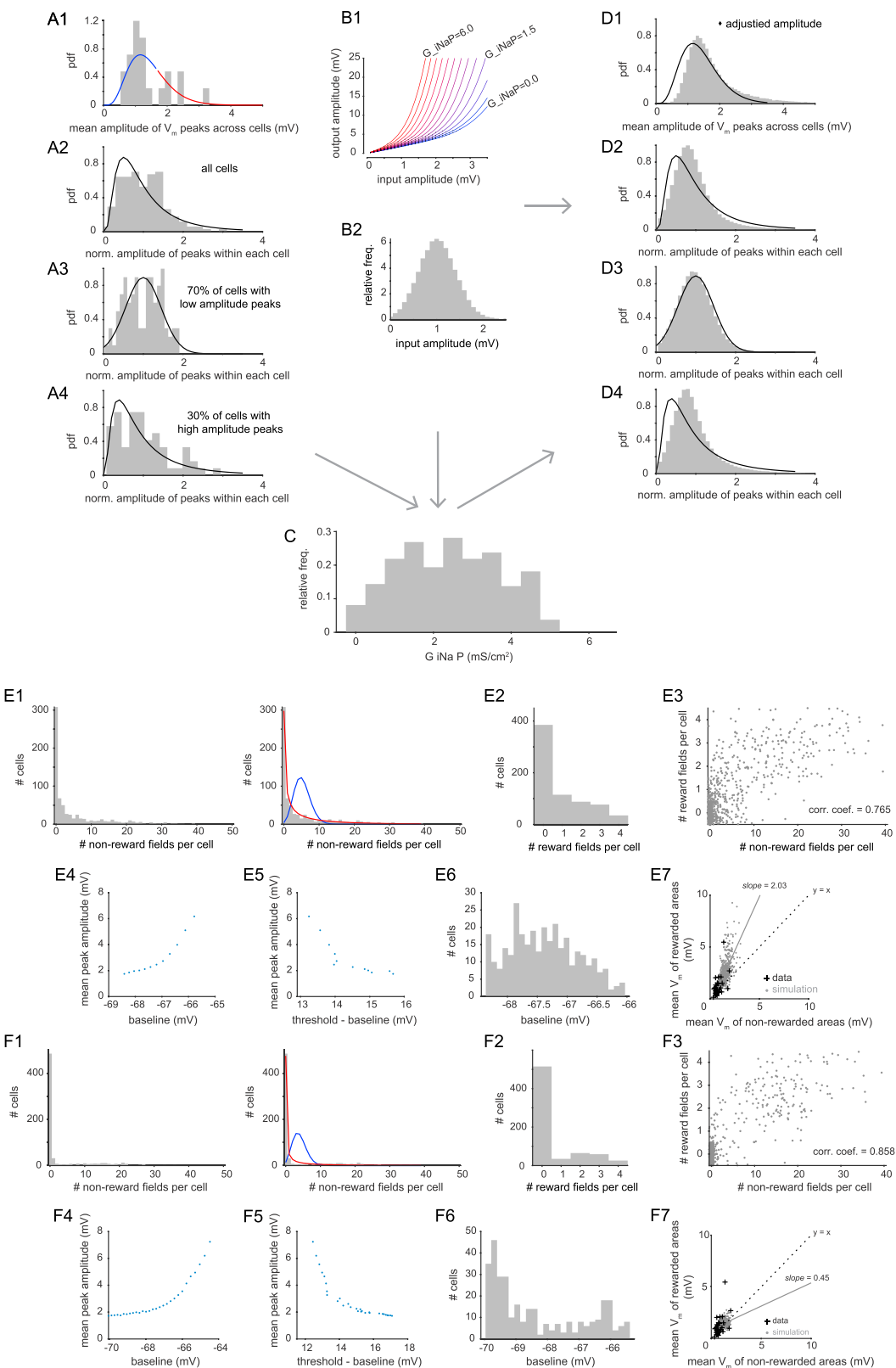


Figure S6. Intracellular Activity of Hippocampal CA1 Neurons Recorded in Head-Fixed Mice Exploring Standard-Sized Virtual Environments Can Account for the Field Propensity Distribution Observed with Imaging in Large Virtual Environments, Related to Figure 7

(A) Average subthreshold V_m (after any APs and related activity were removed) across multiple laps around familiar ~ 2 m virtual tracks as a function of spatial location for 21 cells in 28 sessions (using whole-cell recording). Thin gray box indicates cases where the same cell was recorded in multiple sessions. Red asterisks indicate subthreshold V_m peaks, black dotted lines indicate AP threshold, and gray lines indicate baseline V_m in each session. (B) Distribution of mean of amplitudes of V_m peaks for the individual cells ($n = 21$) (same as Figure 7G). (C) Variance of amplitudes of V_m peaks within a cell (blue circle) versus shuffles (gray dots, $n = 1000$; black, mean \pm s.e.m., $p = 6.08e-42$) in which peaks from all cells were randomly assigned to each cell, showing that cells have significantly different average peak amplitudes. (D) Plot of mean peak amplitude as a function of average baseline V_m for each cell (left) and the histogram of baseline values across the 21 cells (right). (E) Plot of mean peak amplitude as a function of AP threshold – baseline for each cell (left) and the histogram of threshold values across

(legend continued on next page)

the 21 cells (right). (F) Scatterplot of average V_m in rewarded areas versus non-rewarded areas in each cell (same as Figure 7H). (G) Histogram of mean peak amplitude across the 21 cells scaled by each cell's threshold – baseline value (left) and histogram of normalized amplitude of peaks within cells (normalized by each cell's mean peak amplitude) and pooled across all cells (right). (H) Non-reward (left) and reward (middle) field number per cell distributions from simulation of activity in 3 ~40 m environments with 4 rewarded areas each based on parameters derived from these intracellular recordings. Red: gamma-Poisson fit, blue: equal-Poisson fit. Scatterplot of number of reward and non-reward fields per cell from simulation (right). (Left and middle plots are same as in Figure 7I.) See methods.



(legend on next page)

Figure S7. Biophysical Model of Neuron with Conductances and Inputs Fit to Intracellular Data from Figure S6 Can Account for the Observed Field Propensity Distribution, Related to Figure 7

(A1) The probability density function (pdf) of the distribution of mean peak subthreshold V_m amplitude per cell (similar to Figure S6B except smaller binsize to more clearly distinguish higher and lower amplitude cells), fit with gamma distribution. (A2) The pdf of the distribution of normalized peak amplitude, where each cell's peaks are normalized by that cell's mean peak amplitude then all the values are pooled across all 21 cells and fit with log-normal distribution. (A3) Similar to A2 but only including normalized peaks from cells with lower mean peak amplitude in A1 (15 out of 21 cells, blue in A1), fit with Gaussian distribution. (A4) Similar to A2 but only including normalized peaks from cells with higher mean peak amplitude in A1 (6 out of 21 cells, red in A1), fit with log-normal distribution. (B1) Input-output curves of peak subthreshold V_m for 2 s raised cosine inputs provided to neuron with different values of persistent sodium conductance (G_{iNaP} , from 0.0 to 6.0 mS/cm²) simulated using DynaSim. (B2) Distribution of peak amplitudes for input (Gaussian, based on Gaussian distribution of peaks observed in low amplitude cells in (A3)). (C) The pdf of the distribution of G_{iNaP} that best fit (A1-4) using iterative search process (mean = 2.50 mS/cm²). (D1-4) Similar to (A1-4) except from simulations using the G_{iNaP} distribution in (C). Peak amplitudes in D1 were adjusted by -0.7 mV (i.e., D1 shows values after -0.7 mV adjustment) to better allow comparison of shape of distribution with A1 as simulation parameters did not allow as low amplitudes (relative to baseline) as observed in the data. (E1-7) Place field simulation results for a ~40 m environment with 4 rewarded areas (56 non-reward locations and 4 rewarded location, with each location represented as a 2 s raised cosine input) using DynaSim model of a population of 700 cells with G_{iNaP} distribution in (C), input distribution per location given by (B2), and an additional 0.35 mV input added in rewarded areas. (E1) Non-reward field number distribution per cell (red: gamma-Poisson fit, blue: equal-Poisson fit). (E2) reward field number distribution per cell. (E3) Scatterplot of number of reward and non-reward fields per cell. Plot of mean of simulated peak amplitudes as a function of baseline membrane potential (E4) or as a function of threshold – baseline (E5). (E6) The distribution of the baseline of the simulated cells. (E7) Mean V_m in rewarded versus non-rewarded areas, averaged across the 2 s raised cosine, showing multiplicative relationship (solid line: linear regression). (F1-7) Similar to (E1-7) but for a simulation in which G_{iNaP} is the same across all cells (2.50 mS/cm²) and the difference between cells given by different amounts of DC offset added to input (from 0 to 3.0 mV). See STAR Methods.